







Inactive longitude and superflare in the active single-lined pre-main sequence binary V2279 Cyg

XUEYING HU ^{1,2} TIANQI CANG ¹ JIAN-NING FU^{1,2,3} XUAN WANG ^{1,2} KEYU XING,¹ HAOTIAN WANG ¹
PASCAL PETIT ⁴ JIAXIN WANG,⁵ YONG YANG,⁶ AND HE ZHAO ⁷

¹*School of Physics and Astronomy, Beijing Normal University, Beijing 100875, People's Republic of China*

²*Institute for Frontiers in Astronomy and Astrophysics, Beijing Normal University, Beijing 102206, People's Republic of China*

³*Xinjiang Astronomical Observatory, Chinese Academy of Sciences, Urumqi 830011, Xinjiang, China*

⁴*Institut de Recherche en Astrophysique et Planétologie, Université de Toulouse, CNRS, CNES, 14 avenue Edouard Belin, Toulouse, 31400, France*

⁵*School of Science, Chongqing University of Posts and Telecommunications, Chongqing 400065, China*

⁶*School of Physical Science and Technology, Kunming University, Kunming 650214, People's Republic of China*

⁷*Purple Mountain Observatory and Key Laboratory of Radio Astronomy, Chinese Academy of Sciences, 10 Yuanhua Road, Nanjing 210033, China*

ABSTRACT

Young, solar-like stars in the pre-main sequence (PMS) stage exhibit vigorous magnetic activity that significantly influences their circumstellar environments and the processes of planetary formation and evolution. In binary systems, tidal forces and magnetic interactions can further shape the magnetic geometry. We report a longitudinal preference of star spots, chromospheric activities, and flares in the active single-lined spectroscopic PMS binary system V2279 Cyg, based on long-term photometric observations from *Kepler* and *TESS* alongside spectroscopic data from LAMOST. The system is classified as a weak-line T Tauri binary, with component masses estimated at $0.86 M_{\odot}$ and $0.27 M_{\odot}$. V2279 Cyg's nearly circular orbit is synchronized with its 4.126-day rotational period. Observations reveal large star spot regions clustered near the far-side hemisphere. Spectroscopic data show strong, double-peak H α emission, the strength of which is highly correlated with star spot distribution, indicating the presence of an active longitude on the primary star. We also mapped the prominence structure co-rotating with the primary star, suggesting a dense structure close to the near-side hemisphere. Furthermore, we identify an inactive longitude of flares during the 4-year *Kepler* observations, where the frequency of flare activity is significantly reduced after the superior conjunction, marking the first such identification in active binary systems. Additionally, a white light superflare, releasing energy of 2.5×10^{37} erg, was detected in *TESS* observations. These findings provide valuable insights into the magnetic field geometry and dynamo processes in PMS binaries, underscoring the critical role of tidal interactions in shaping magnetic activities.

Keywords: stars: binaries, stars: flare, stars: pre-main sequence, stars: activity, individual: V2279 Cyg

1. INTRODUCTION

Young, solar-like stars in the pre-main sequence (PMS) stage offer opportunities to study the early phases of stellar and planetary evolution. During this stage, stars exhibit strong magnetic activity driven by dynamo processes in their convective envelopes (Hussain & Alecian 2014). This activity manifests in phenomena such as star spots, flares, prominences, and stellar winds, which can significantly influence their circumstellar environments and, by extension, the formation and evolution of planetary systems (Gallet et al. 2017). Among PMS stars, T Tauri stars (TTs) are particularly useful for investigating magnetic activity and its impact on stellar evolution. TTs, typically a few million

years old and with masses ranging from 0.2 to 2 M_{\odot} , are categorized into two subclasses: classical T Tauri stars (cTTs), which exhibit significant accretion from circumstellar disks, and weak-line T Tauri stars (wTTs), which show minimal to no accretion activity and have largely dissipated their surrounding circumstellar material.

The activity level of a star is related to its rotation. In general, the more rapidly the star rotates, the higher the magnetic activity can be observed. However, when the rotation is rapid enough, the activity level reaches the upper limit and does not increase with the more rapid rotation. This so-called saturated regime has been highlighted for PMS stars with X-ray (Argiroffi et al. 2016), and other active stars (e.g., Vidotto et al. (2014)). Theoretical attempts and simulations on this phenomenon remain flawed (Guerrero et al. 2019; Wei 2022).

In wTTs, magnetic activity is primarily influenced by rapid stellar rotation and dynamo processes. These stars often exhibit strong magnetic fields, with strengths reaching kilo-Gauss levels in systems like V410 Tau (Skelly et al. 2010; Carroll et al. 2012), V830 Tau (Donati et al. 2015), LkCa 4 (Finociety et al. 2023), and TWA 6 & 8A (Hill et al. 2019). This magnetic activity gives rise to rotationally modulated light curves due to star spots and frequent flaring events (e.g., Fernández et al. 2004). Components in close binaries also perform rapid rotation, leading to significant stellar activities (Gunn et al. 1998). Observations of magnetic activity in close binaries suggest that spots can sometimes cluster at specific stellar longitudes or the so-called active longitudes, leading to a preference for certain regions of enhanced activity (Berdyugina et al. 1998). For a tidally locked system, this longitude preference is bound to the rotational phase (Oláh 2006; Toledano et al. 2007), and tends to appear at sub- and anti-stellar points (Sethi & Martin 2024). The dynamo processes responsible for generating these stable, non-axisymmetric fields are influenced by rapid rotation, which is sustained through tidal interactions in binary systems (Moss & Tuominen 1997; Berdyugina 2005).

Active longitudes are highly related to the region where flares occur on the Sun (Gyenge et al. 2016). However, the distribution of flare events in close binary systems is random (Huang et al. 2020c). The understanding of energy transfer between magnetic field structure and flares, especially considering the magnetic field and tidal interactions for close binaries, is still rough. Moreover, the enhanced stellar activity in close binaries (Johnstone et al. 2019; Oláh et al. 2021) may influence the formation and habitability of planets, and contribute to the magnetic evolution of close-in giant planets.

V2279 Cyg ($\alpha_{2000} = 19 : 18 : 54.46$, $\delta_{2000} = +43 : 49 : 25.88$) is an intriguing binary system for investigating longitude preference in a young, active environment. Initially classified as a classical Cepheid variable (Akerlof et al. 2000) and later as an RS CVn-type binary (Dahlmark 2000). V2279 Cyg has been extensively monitored by space-based photometric missions, including *Kepler* mission (Koch et al. 2010) and *Transiting Exoplanet Survey Satellite* (*TESS*, Ricker et al. 2015). According to multi-color photometric and high-resolution spectroscopic analyses by Szabó et al. (2011), V2279 Cyg has different performance from a Cepheid, especially in its strong magnetic activity signatures and amplitude ratios in different bands. These observations reveal strong rotational modulation consistent with star spots and frequent flaring events, providing an opportunity to study the distribution and evolution of magnetic activity in the system.

In this paper, we analyze photometric and spectroscopic data from V2279 Cyg to investigate the longitude preference of star spots and flares. We identified regions of enhanced magnetic activity and assessed their persistence over time. In Section 2, we describe the observations and data reduction. Section 3 focuses on constraining the system’s stellar and orbital parameters. In Section 4, we model the spotted region, reconstruct prominence maps, and analyze the longitude preference of star spots and flares. Finally, we discuss their implications in Section 5 and summarize our results in Section 6.

2. OBSERVATIONS

Photometric monitoring data for V2279 Cyg retrieved from the Mikulski Archive for Space Telescopes (MAST¹), was collected by *Kepler* (KIC 8022670, from 2009 - 2013, doi:10.17909/t9488n) and *TESS* (TIC 159106204, 2019 - now, doi: 10.17909/t9-nmc8-f686) mission. We employed *Kepler* long-cadence light curves (LCs; 1800s exposure time) from Quarters 0 to 17, and *TESS* light curves processed with the official Quick-Look Pipeline (QLP; Huang et al. 2020a,b; Kunimoto et al. 2021, 2022). This *TESS* observations span multiple sectors, but generally belong to 3 epochs: Sector 14 (Jul 18 to Aug 14 2019), Sectors 40 ? 41 and 54 ? 55 (Jun 25 to Aug 20 2021 & Jul 9 to Sep 1 2022), and Sector 74 - 75 & 80 (Jan 3 to Feb 12 2024 & Jun 18 to Jul 14 2024). Time-resolved spectroscopic observations were carried out

¹ <https://mast.stsci.edu>

Table 1. Basic stellar parameters of V2279 Cyg from different sources of photometric and spectroscopic observations in optical and infrared. The abbreviation and corresponding references are listed in the references.

	B20	F16	F22	Z20	T19	L19	S11
Data source	Board bands	LAMOST	LAMOST	LAMOST	APOGEE	APOGEE	TREM
Spec domain	Optical	Optical	Optical	Optical	Infrared	Infrared	Optical
T_{eff} (K)	4772	4651	4985	4557	4984	4651	4900
$\log g$ (dex)	3.256	2.96	2.64	3.07	4.388	3.10	3.7
[Fe/H]	-0.043	-0.08	-0.06	-0.262	-0.391	-0.5	-1.2

References— B20: Berger et al. (2020), F16: Frasca et al. (2016), F22: Frasca et al. (2022), Z20: Zong et al. (2020), T19: Ting et al. (2019), L19: Leung & Bovy (2019), S11: Szabó et al. (2011)

by the Large Sky Area Multi-Object Fiber Spectroscopic Telescope (LAMOST), as part of the LAMOST-*Kepler*/K2 project (De Cat et al. 2015; Zong et al. 2018b, 2020; Wang et al. 2020; Fu et al. 2020). V2279 Cyg was observed extensively between 2018 and 2020, resulting in a total of 71 medium-resolution ($R \sim 7,500$) spectra from LAMOST Data Releases 6, 7, and 8, with signal-to-noise ratios (S/Ns) greater than 7. The wavelength coverage is divided into the red arm ($\lambda \in [630, 680]$ nm) and the blue arm ($\lambda \in [495, 535]$ nm).

The brightness variations observed in these light curves are primarily attributed to rotational modulation caused by star spots (Oláh et al. 2021). Using the Lomb-Scargle method, with a signal-to-noise ratio (S/N) threshold of 100, we extracted the primary period of approximately 4.13 days, and a much weaker secondary signal of 2.06 days, which is half the primary one. We note that the rotational modulation pattern in both *Kepler* and *TESS* light curves appears unstable, likely due to the evolution of star spots. This leads to variations in the modulation pattern shape across cycles, as shown in the phase-folded light curves (Fig. 1a & b). The variation of pattern can further affect the determination of period since extra frequencies are included to fit the change of light curve shape. In this case, determination and any long-term analysis of the period should consider the variation of the light curve.

Since the light curve shape of *Kepler* data is stable enough, in order to reduce the effect of light curve shape variation, we conducted a time-frequency analysis using the method described in Zong et al. (2018a), extracting the frequency around the main period by applying a sliding Lomb-Scargle periodogram (sLSP) analysis with a window width of 200 days and a time step of 5 days. The primary period is relatively stable in the 4-year observation with $P_{\text{rot}} = 4.1264 \pm 0.0001$ days (Appendix. A). Using this period, we derived the following ephemeris:

$$\text{BJD} = \text{BJD}_0 + 4.1264(1)E, \quad (1)$$

where $\text{BJD}_0 = 2458268.3132 \pm 0.0056$ was selected corresponding to the inferior conjunction between two LAMOST observing nights, corrected for light travel time to the solar system’s barycenter (Li et al. 2019), and E the cycle number. As shown in Fig. 1b, this ephemeris works for *TESS* data, and the patterns in different years are concentrated.

To extract radial velocities (RVs) from the LAMOST spectra, we used the *laspec* package (Zhang et al. 2021). RVs were measured separately for the red- and blue-arm spectra. The folded RV curves, based on the ephemeris derived in Eq. 1, are shown in the bottom panel of Fig. 1. The spectroscopic analysis classifies the system as a single-lined spectroscopic binary (SB1). We fitted the RV curve using a single sinusoid function with an RV amplitude of approximately 32 km s^{-1} , suggesting that the orbital period of the system is nearly identical to the rotational period of the primary star. Additionally, the system’s orbital eccentricity is inferred to be close to zero, indicating a nearly circular orbit.

3. STELLAR PARAMETERS AND EVOLUTIONARY STAGE

We collected measurements of the basic stellar parameters (T_{eff} , $\log g$ and [Fe/H]) for V2279 Cyg from seven sources, as summarized in Table 1. Among these, Berger et al. (2020) used broadband photometry, luminosity, and spectroscopic metallicities from Gaia and *Kepler* data, thus providing a reference for the determination of T_{eff} and $\log g$. All of the measurements indicate that V2279 Cyg is a cool star with $T_{\text{eff}} < 5000 \text{ K}$.

In such temperature range, infrared spectra are less influenced by spotted regions and offer a larger number of lines available for measuring chemical abundances. V2279 Cyg was observed by the APOGEE survey (Majewski et al. 2017, ID: 2M19185446+4349258), which offers high-resolution data ($R \sim 22,500$) in infrared band. From APOGEE observations, two independent [Fe/H] measurements point to a low metallicity for V2279 Cyg (-0.391 from Ting et al.

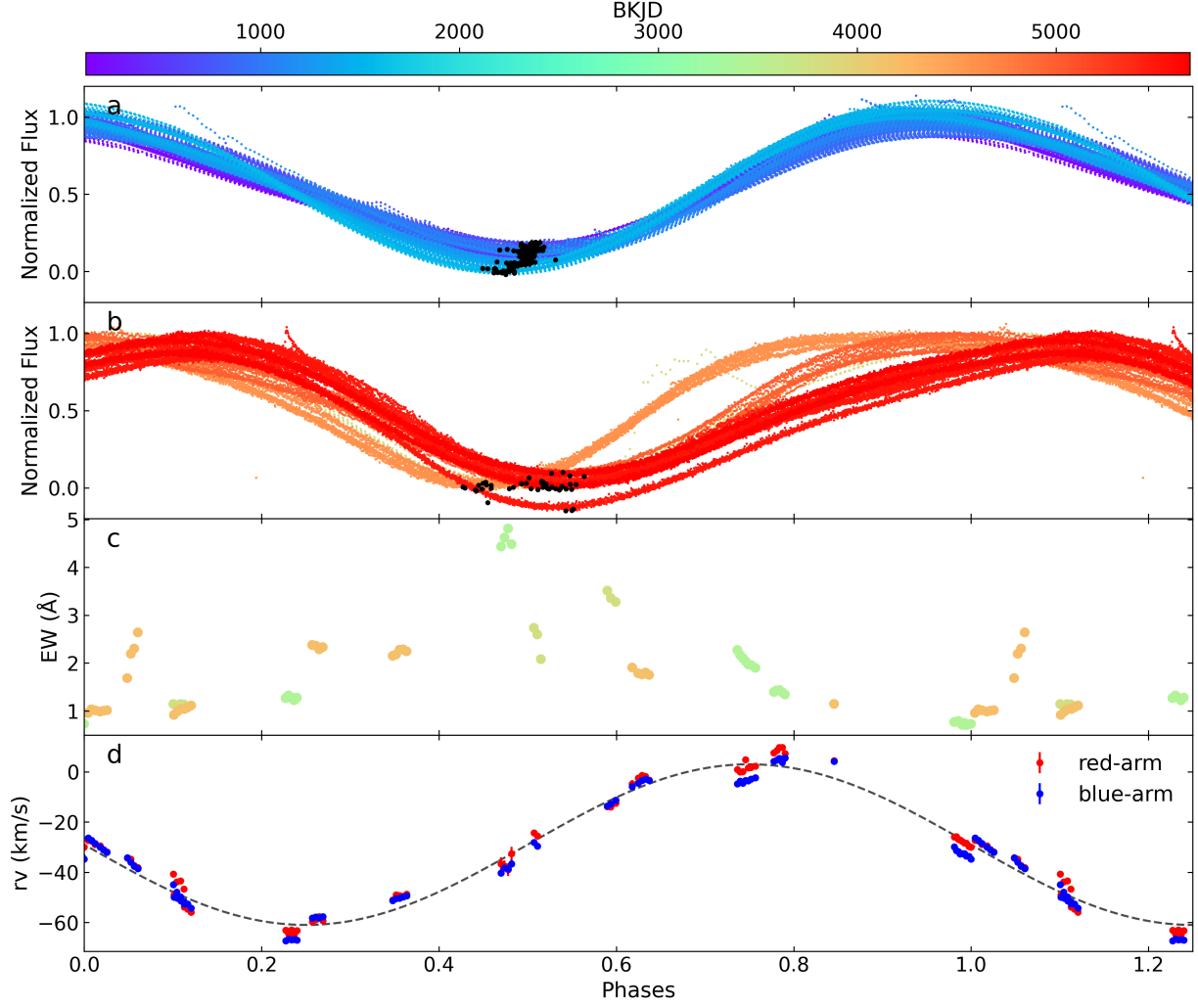


Figure 1. The phase-folded curves for V2279 Cyg. (a) *Kepler* light curve. The red dots mark the minimum value in each cycle. (b) *TESS* light curve. The red dots mark the minimum value in each cycle. (c) The equivalent widths (EWs) of H α line for V2279 Cyg from LAMOST MRS. The colorbar for (a-c) represents the Barycentric Kepler Julian Date (BKJD). (d) RV curves of V2279 Cyg, where the red dots represent the RVs measured from the H α lines of the red-arm spectra (RV_r), and the blue dots from the metal lines of the blue-arm spectra (RV_b). Table 3 in Appendix B lists the RV_r and RV_b. The black dashed line is the sine fitting result using the average value of the data from both arms.

2019 and -0.5 from Leung & Bovy 2019, respectively). However, the $\log g$ from Ting et al. (2019) is too large to match the luminosity. Meanwhile, ROTFIT pipeline (Frasca et al. 2016) for LAMOST data tends to overestimate [Fe/H] in metal-poor stars (Frasca et al. 2022), which suggests that there could be a systematic bias in the derived $\log g$ for V2279 Cyg.

Additionally, Szabó et al. (2011) derives an even lower metallicity [Fe/H] = -1.2 from a high-resolution ($R = 48,000$, 390–740 nm) TRES spectrum. However, this measurement relies on fitting theoretical template spectra over a relatively limited spectral range, and strong chromospheric emission lines may have affected the fitting. To account for spot effects, we used the LASP pipeline (Wu et al. 2014) to extract stellar parameters from each LAMOST spectrum acquired at different epochs, instead of the average value from Zong et al. (2020). We adopted $T_{\text{eff}} = 4596 \pm 44$ K, $\log g = 3.149 \pm 0.045$ and [Fe/H] = -0.217 ± 0.029 from the phase $\phi = 0$, corresponding to the star’s brightest phase (i.e., minimal spot coverage). These values are generally consistent with those reported by Leung & Bovy (2019), who found $T_{\text{eff}} = 4651 \pm 115$ K, $\log g = 3.10 \pm 0.35$ and [Fe/H] = -0.5 ± 0.1 . Therefore, we adopt these parameters from APOGEE throughout our subsequent analysis.

Table 2. System parameters of V2279 Cyg.

Parameters	Values	Ref.
Period (d)	4.1264 ± 0.0001	This work
T_{eff} (K)	4651 ± 115	1
$\log g$ (dex)	3.10 ± 0.35	1
[Fe/H]	-0.5 ± 0.1	1
$v \sin i$ (km/s ⁻¹)	43.2 ± 3.2	2
M_1 (M_{\odot})	0.86 ± 0.12	This work
M_2 (M_{\odot})	0.27 ± 0.03	This work
Radius (Primary) (R_{\odot})	3.64 ± 0.36	This work
e	^a 0	This work
INCL (°)	^a 75	This work
R_{orb} (R_{\odot})	^a 11.2	This work
L (L_{\odot})	5.59 ± 0.08	This work
V magnitude (^{mag})	12.7	3
G magnitude (^{mag})	12.6	4
A_G (^{mag})	^a 0.37	This work
Distance (pc)	696 ± 5	4

NOTE—^a Fixed values

References— 1.Leung & Bovy (2019), 2.Frasca et al. (2022), 3.Pigulski et al. (2009), 4.Gaia Collaboration (2020).

Based on the stellar parameters derived above (Table 1), we estimated the mass of the primary component of V2279 Cyg using the luminosity derived from Gaia astrometric observations (Vincent et al. 2020) and stellar evolutionary models. The absolute magnitude $M_G = 3.02$ in the Gaia G-band was determined using the Gaia parallax π and the corresponding apparent G magnitude m_G . To account for extinction, we used the monochromatic extinction at 541.4 nm (A_0) derived from the recently released 3D dust map by Dharmawardena et al. (2024)². The extinction in the G-band was calculated as $A_G = 0.37$, considering the non-linear effects of the stellar spectral energy distribution (SED) and the filter transmission (see detailed discussions in Li & Chen 2023; Maíz Apellániz 2024).

To constrain the mass of the primary star, we employed the MIST³ stellar evolutionary tracks (Dotter 2016; Choi et al. 2016), computed with the Modules for Experiments in Stellar Astrophysics (MESA) code (Paxton et al. 2011, 2013, 2015). By comparing T_{eff} and $\log g$ with the evolutionary tracks and using M_G as a constraint, we derived a primary mass of $M_1 = 0.84 \pm 0.12 M_{\odot}$ based on M_G , and $M_1 = 0.86 \pm 0.12 M_{\odot}$ based on $\log g$ (uncertainty taken from the interpolation of grids). Both results confirm that the primary star is a pre-main sequence (PMS) star, as shown in Fig. 2.

As for the secondary component, we adopted the binary mass function, assuming that the eccentricity of the orbit is $e = 0$, we have

$$f = \frac{M_2^3 \sin^3 i}{(M_1 + M_2)^2} = \frac{P_K^3}{2\pi G}. \quad (2)$$

A sinusoidal fit to the radial velocity points (Fig. 1 d) gave the peak radial velocity $K \sim 32$ km/s. Frasca et al. (2022) measured the $v \sin i$ for V2279 Cyg as 43.2 km/s. From $L = 4\pi R^2 \sigma T^4$, we estimated the radius for the primary star as about $R_1 = 3.64 \pm 0.36 R_{\odot}$. Here, the bolometric luminosity $L_{\text{bol}} = 5.59 \pm 0.08 L_{\odot}$ is derived by:

$$-2.5 \log L_{\text{bol}} = M_G + \text{BC}_G - M_{\text{bol}, \odot}, \quad (3)$$

where $\text{BC}_G = -0.15$ is estimated by the bolometric correction tool for the Gaia DR3 G-band (Creevey et al. 2023) with the T_{eff} , $\log g$, and [Fe/H]. $M_{\text{bol}, \odot} = 4.74$ is the bolometric luminosity of the Sun (Mamajek et al. 2015). We can then estimate the equatorial velocity $v_{\text{eq}} = 44.6$ km/s. Taking the projected equatorial velocity $v \sin i = 43.2 \pm 3.2$ km/s from the LAMOST mid-resolution spectra (Frasca et al. 2022), we obtained an estimation of the rotational

² The dust map is accessible online at <https://zenodo.org/records/11448780>.

³ <http://waps.cfa.harvard.edu/MIST/index.html>

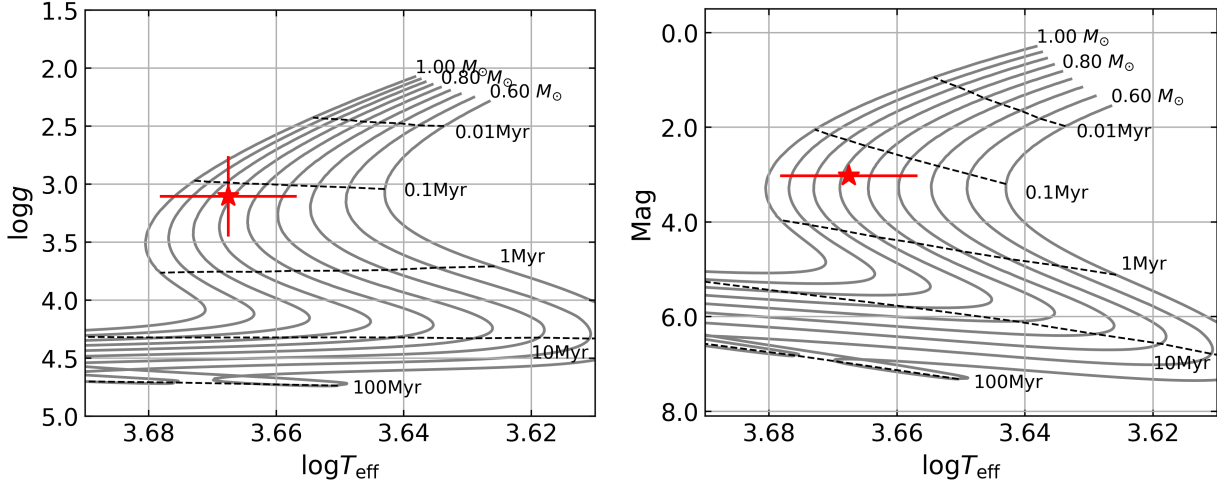


Figure 2. Evolutionary tracks from MIST with input masses between 0.6 and 1 M_{\odot} (step: 0.05 M_{\odot}) and $[\text{Fe}/\text{H}]$ of -0.5. The red star marks the position of the primary component with error bars. The black dotted lines are isochrones.

inclination angle of $i \sim 75^{\circ}$. Thus the mass of the secondary component is $M_2 = 0.27 M_{\odot}$, and the radius of the orbit $R_{\text{orb}} = 11.3 R_{\odot}$. Since the more massive component does not reach the main sequence, the secondary component should also be a pre-main sequence star. All stellar parameters used in this study are summarized in Table 2.

4. PREFERENCE LONGITUDES OF SPOTS AND FLARES

4.1. Spotted region

Over the *Kepler* observation period (2009 - 2013), the variation in the light curve shape was minor, with the phase of the brightness minimum remaining roughly consistent at around $\phi \sim 0.5$ from cycle to cycle as shown in Fig. 1. This suggests that the overall brightness distribution on the surface of the primary star was generally stable, i.e., the active longitude was facing the secondary star. For the *TESS* data, the phase-folded light curves exhibit three rotation modulation shapes corresponding to three distinct observation epochs (2019, 2021-22, 2024). Although a bit extended, the brightness minimum is also located between 0.45 and 0.55, keeping the same active longitude as *Kepler* data. A single-peak, continuous modulation pattern appears in all cycles of *Kepler* and *TESS* observations, indicating a large spotted region facing the secondary star that transits the surface with stellar rotating. Further confirmation can be obtained using both the two-spot model and line profile asymmetries. Since the evaluation of the location of the spotted region is sensitive to the rotational phase (or longitude), the preference of the spotted region can be concluded as active longitude, like other binaries.

We examined variations in the spectral line profiles, thanks to the large projected equatorial velocity ($v \sin i$) of V2279 Cyg, which provides spatial information about the surface brightness distribution (Vogt & Penrod 1983). However, due to the limited resolution and S/N of the spectra, direct detection of line profile distortions caused by star spots in individual spectral lines was challenging.

To address this, we employed the Least-Squares Deconvolution (LSD) technique (Donati et al. 1997), implemented via the Python-based routine LSDpy⁴ (Folsom et al. 2018), to compute average pseudo-line profiles and enhance the S/N. For the LSD analysis, a line mask was constructed using a typical list of photospheric absorption lines (strong chromospheric lines are excluded) for stars with $T_{\text{eff}} = 4750$ K and $\log g = 3.0$, selected from the Vienna Atomic Line Database (VALD) (Piskunov et al. 1995; Kupka et al. 1999). The LSD profiles were computed with a velocity step of 15 km s⁻¹, slightly smaller than the velocity step of the LAMOST medium-resolution spectra. Figure. 15 in Appendix. F shows the LSD profiles for all rotational phases of V2279 Cyg’ spectra, corrected for radial velocity. To isolate surface brightness variations, the mean photospheric structure, modeled as a Gaussian profile, was subtracted from all LSD profiles as shown in Fig. 3. A large portion of residual profiles shows an antisymmetric structure with opposite signs on the red and blue sides, indicating the presence of a large spotted region.

⁴ <https://github.com/folsomcp/LSDpy>

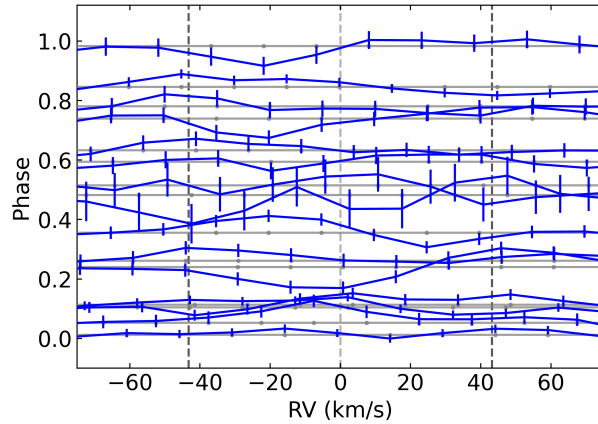


Figure 3. Difference between LSD profiles and the Gaussian fitting (gray horizontal lines) of the mean LSD profile. The vertical gray dashed lines mark the $\pm v \sin i$. Uncertainties (vertical blue lines) are estimated with the LSD process from the observational uncertainty.

Assuming fixed orbital parameters for the V2279 Cyg binary system as described in Sect. 3, we modeled the star spots on the surface of the primary component using the PHysics Of Eclipsing BinariEs (PHOEBE) software, version 2.4⁵ (Prša & Zwitter 2005; Prša et al. 2016; Horvat et al. 2018; Jones et al. 2020; Conroy et al. 2020).

The modeling employed the built-in Markov Chain Monte Carlo (MCMC) method, implemented via the `emcee` package (Foreman-Mackey et al. 2013), to fit the light curve and derive a two-spot solution (parameters listed in Table 2). For simplicity, we focused on the *Kepler* Quarter 1 (Q1) data, assuming minimal changes in the light curve over time. As shown in Fig. 1, the light curve variations in other quarters are minor, and the Q1-derived model is applicable to them as well.

The resulting model, shown in Fig. 4, identifies two large, dark spots with an overlapping region near the pole, creating an even darker area. This configuration reproduces the observed light curve well. The spots remain visible throughout the rotational cycle, consistent with the LSD analysis, which reveals absorption line asymmetries in all the observations.

Although a two-spot model can fit the spot-modulated light curve, which is in agreement with other spot modeling of wTTSs (Lanza et al. 2016; Xu et al. 2021), the actual brightness distribution can be much more complex, as shown by Doppler imaging (e.g., LkCa 4 by Finociety et al. (2023) provided an example for fitting photometry and spectroscopic data simultaneously). Furthermore, the two-spot model can be highly impacted by the degeneration of parameters and create spurious parameters (Jeffers 2005), which may lead to the difficulty of converging parameters in the MCMC method. There are many local minima in the MCMC sampling in our modeling that walkers converge quickly into one of them (see Fig. 11). However, this toy model still provides global information that the heavily spotted area covers a large region of the V2279 Cyg surface. The spectral line distortion also indicates that a large spotted region transits the disk, which confirms the conclusion from the light curve.

4.2. Longitude preference of flares

The occurrence of flares is also believed to correlate with active regions dominated by star spots for wTTSs (e.g., Fernández et al. 2004; Nicholson et al. 2018). A total of 43 flares were identified in the *Kepler* dataset (Quarters 0?17) by Oláh et al. (2021, 2022). For the *TESS* data, we employed a flare detection tool designed explicitly for *TESS* light curves, developed by Xing et al. (2024), and identified 10 additional flares for V2279 Cyg. To estimate the energy of the flares detected in the *TESS* data, we followed the method described in Vida & Roettenbacher (2018) and used the flare analysis routines provided by Xing et al. (2024). The method obtained bolometric flare energy by correcting the effect of the *Kepler* and *TESS* passbands, respectively. The calculated flare energies are listed in Appendix D. As shown in the phase-folded flare energy distribution in Fig. 5, **NO** flare was detected in the *Kepler* data within the phase range of 0.60 to 0.78, except a superflare observed in *TESS* Sector 14 and covered almost the gap. Assuming that the occurrence of flares is generally random, the 43 *Kepler* flares indicate a likelihood of $< 0.03\%$

⁵ <http://phoebe-project.org>

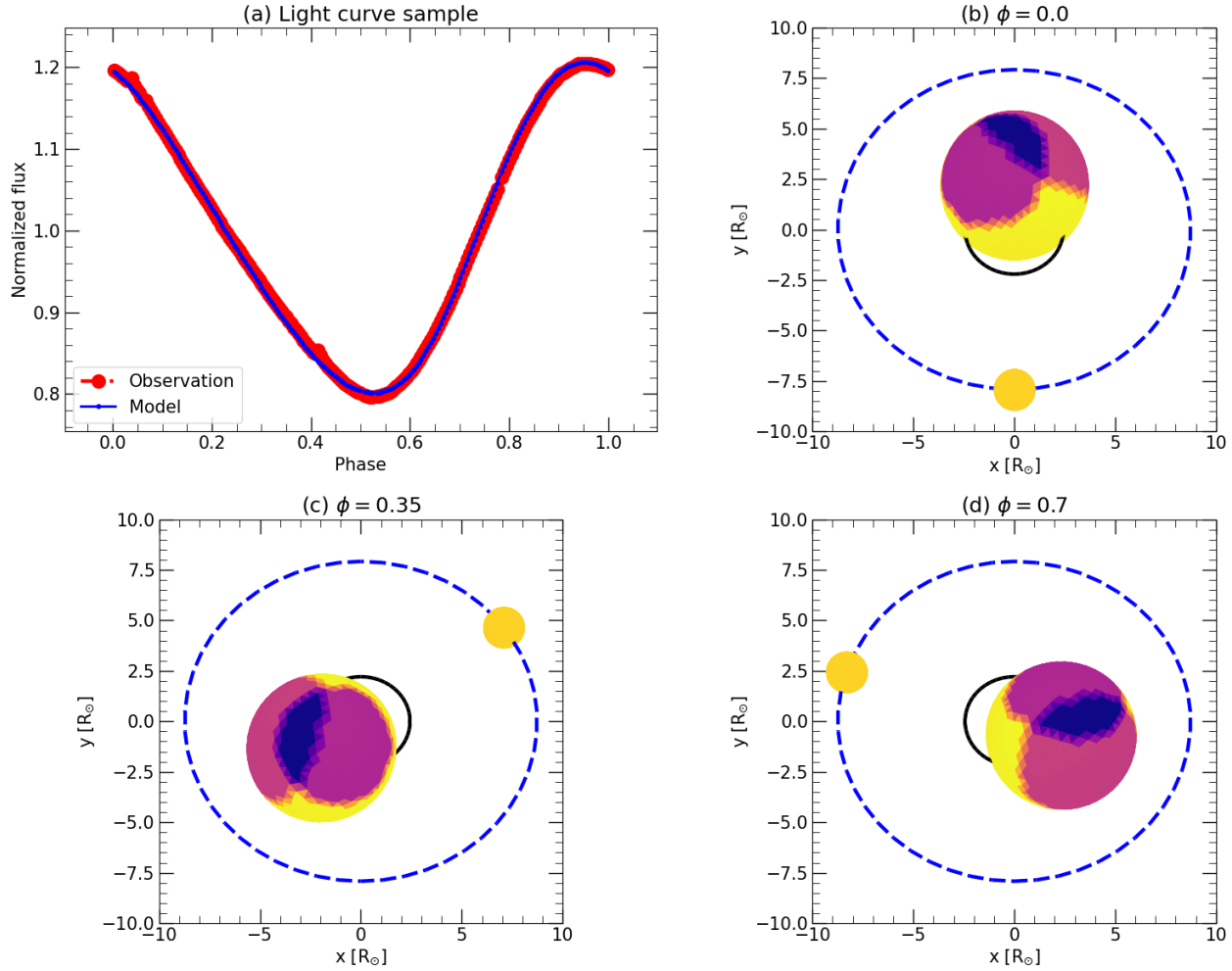


Figure 4. The spot model to fit the light curve of *Kepler* Q1 data set. (a) The normalized flux in the phase-folded diagram for the model (blue line) and observations (black dot). (b-d) The configurations of the two-spot model at $\phi=0$, 0.35 and 0.7, respectively. The view illustrates the line-of-sight perspective (considered the inclination) of the two-spot model. Solid lines show the orbit of the primary (black) and secondary (blue) stars.

that no flare would be detected within a 0.18 phase interval during continuous monitoring. In this case, we define this longitude preference of flares as an "inactive longitude". The other *TESS* flares occurred at similar phases to those observed in the *Kepler* light curves, with a likely random distribution. Note that the superflare released an energy of approximately 2.53×10^{37} erg, which is at least an order of magnitude larger than the others (details in Appendix D).

4.3. Asymmetric H-alpha emission

The active longitude is correlated with the chromospheric activity performed by the emission lines in other active binaries (e.g., [Nicholson et al. 2018, 2021](#)). In the red arm of LAMOST medium-resolution spectra, we noticed strong emission as well as profile variations in $H\alpha$ lines. The $H\alpha$ profile was generally the same in one observation run with 1 \sim 9 spectra in 3 hours from LAMOST, which is much shorter than the 4.13-day orbital period. Therefore, the spectral data from observations in a single night are averaged together to improve the S/N (Fig. 16). $H\alpha$ lines are purely emitting, sometimes with two peaks slightly outside the $v \sin i \sim 43$ km/s, e.g., observation on May 30, 2018. In general, the peaks can reach ± 80 km/s, and the whole emission structure can extend to about ± 300 km/s, which is much larger than $v \sin i$. The $H\alpha$ emission on May 31, 2018, was significantly stronger than that at other times, which can be attributed to a flare. The significant stellar activity events on the primary component of V2279 Cyg suggest a strong magnetic field on the stellar surface that can support prominences like other solar-like stars ([Villarreal](#)

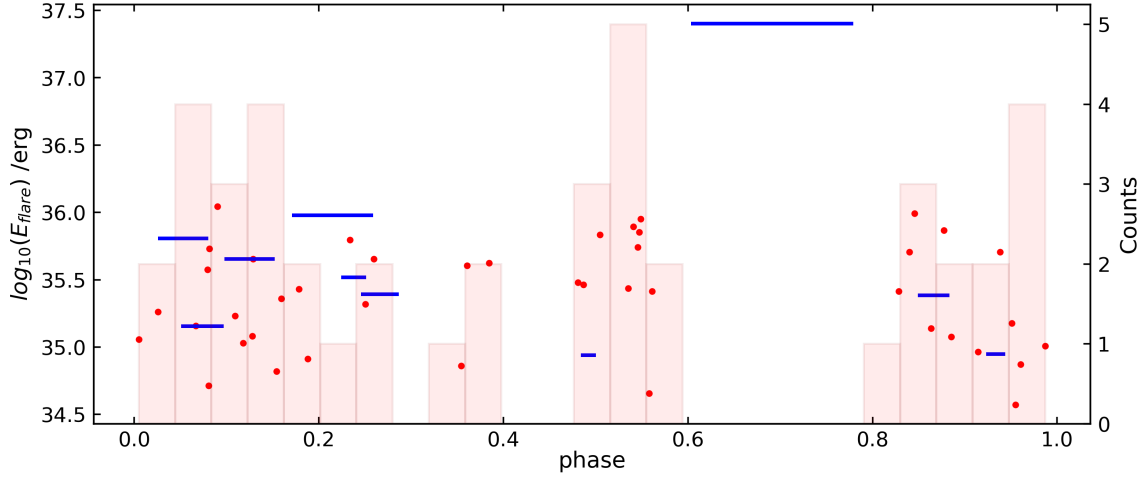


Figure 5. The phase-folded flare energies calculated from *Kepler* LC light curves (Oláh et al. 2022) and *TESS* (our work). The red dots mark the *Kepler* results (at the peak time), and the blue lines represent the *TESS* results (labeling the duration). The light red histogram displays the number of flares at different phases.

D’Angelo et al. 2019). Although young binary stellar systems can host circumstellar or circumbinary discs (Akeson et al. 2019), we attribute the $\text{H}\alpha$ emission of V2279 Cyg to the chromospheric activity due to the ultraviolet excess and no significant infrared excess in SED as shown in Fig. 14, where the infrared observations are taken from WISE (Wright et al. 2010). The enhanced blue peak is also identified in other active wTTSs (Nicholson et al. 2018, 2021), which can be explained by the mass motion towards the observer.

The equivalent width (EW) of $\text{H}\alpha$ lines shows a weak rotational modulation (Fig. 1c). Still, we can recognize a maximum EW at around $\phi = 0.5$ and a minimum EW at around $\phi = 0$, corresponding to the most spotted region and the brightest region of the star. We calculated the Pearson correlation of -0.78 between the variation of EW and the average phase-folded light curve of *Kepler* data, indicating that a more spotted region has a higher chromospheric activity for V2279 Cyg.

One potential scenario of the asymmetric $\text{H}\alpha$ emission in the young active stars without disk can be attributed to the cool, dense gas confined by the strong magnetic field and co-rotating with the stars, or the so-called slingshot prominences (Collier Cameron 1996; Zaire et al. 2021). This scenario can be applied to V2279 Cyg due to the large inclination $\sim 75^\circ$, which results in almost no transit event and absorption features in $\text{H}\alpha$ line profiles - the slingshot prominences can always be seen from the line-of-sight. We notice that in the dynamic spectra for 2020 (Fig. 16), the difference between the line profiles of close phases is minor, with a close position of peaks. For example, the line profile on June 15, 2020, is similar to the one on June 3 after 12 days. We suppose that these repeating profiles indicate a globally stable structure co-rotating with the star in a short-term time duration.

In order to model the co-rotating structure around the primary component, we employed Doppler tomography (Marsh & Horne 1988) for spectra in 2020, assuming that the main prominence structure is generally stable in about two weeks and the emitting materials are optically thin. We used the tomography code developed by Donati et al. (2000), which is based on the algorithm of Marsh & Horne (1988) and was used in other prominence systems (Cang et al. 2020; Petit et al. 2005). The system is assumed to be in a quasi-steady state so that each region of emitting gas maintains a stable velocity in the rotating/orbital frame, and the only change in the observed line profiles (as a function of orbital or rotational phase) is due to the changing line-of-sight. Assuming that the $\text{H}\alpha$ emitting materials are optically thin, we used the local $\text{H}\alpha$ profile of Gaussian shape with a $\sim 15 \text{ km s}^{-1}$ Gaussian FWHM, and located them to the 2D velocity map (V_x, V_y). In the practice of the reconstruction, we neglected the absorption of the star for the detection of hot materials outside the star (Donati et al. 2000). As shown in the dynamic spectrum in Fig. 6, the tomography model (middle panel) roughly fits the pattern of emissions in the observations (left panel), with residuals (right panel) approximately an order of magnitude lower than the observed fluxes. The mismatch mainly happens between $\phi = 0.4$ and $\phi = 0.7$, where is the most spotted region.

The resulting spatial distribution of prominences is shown in Fig. 7, in which the central zero point marks the position of the primary star in the velocity field. In the prominence map, the $\text{H}\alpha$ emitting materials concentrate

mainly at the phase $\phi \sim 0$, near the surface of the primary star, which is close to the brightness maxima of *Kepler* light curve, near the inferior conjunction. Unfortunately, although 2020 provided the largest number of observations among the three seasons, the data were unevenly distributed across the orbital phases. Furthermore, the limited phase coverage from 2018 and 2019 (only 5 and 3 nights, respectively) made it impossible to reconstruct prominence maps for those years, hindering our ability to discern the long-term structures surrounding the primary star and the binary system.

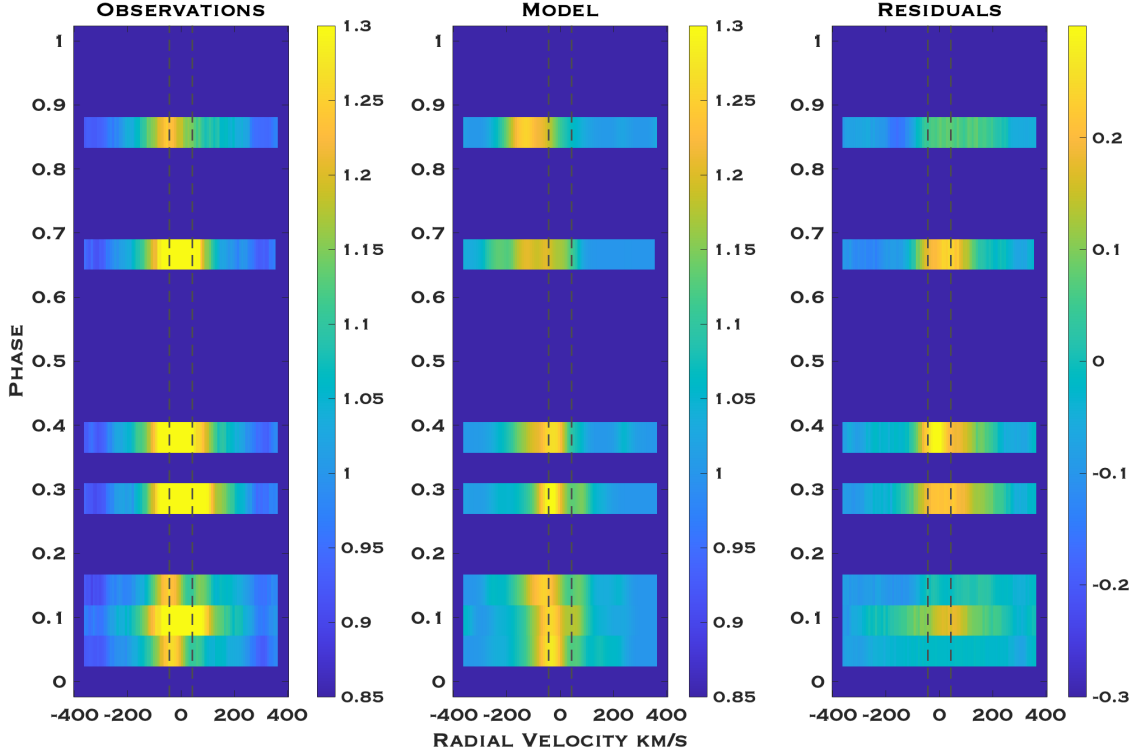


Figure 6. Dynamic spectra showing the H α line of V2279 Cyg (in 2020). From left to right: observations (after correcting the rv caused by the binary system), model and model residual. The vertical black dashed lines mark the $\pm v \sin i$.

5. DISCUSSION

5.1. Evolutionary state of V2279 Cyg

From the MIST evolutionary tracks, we derived the age of V2279 Cyg as ~ 0.16 Myr, which is younger than the typical TTs aged from 0.5–10 Myr, even younger for wTTs that have dissipated their discs. Since we did not find clues for accretion gas around V2279 Cyg, the abnormally determined age of V2279 Cyg is potentially due to the interaction between the components of the binary system. The mass transition in the earlier stage and the potential accreting materials in the orbit plane may be cleared by the tidal effect between the two components (refer to the review by Mathieu (1994)).

The circular orbits and tidal lock found in the V2279 Cyg system widely exist in the other close binary systems with an orbit period of shorter than 7 days (Simonian et al. 2019). Although low-mass binaries in the PMS stage are easier to reach synchronization due to the larger size and convective envelope (Zahn & Bouchet 1989), V2279 Cyg has a very limited time for angular momentum evolution (Gallet & Bouvier 2013), which requires strong tidal torques and magnetic braking to drive the process (Fleming et al. 2019).

Furthermore, the rapid rotation of V2279 Cyg may lead to a saturated dynamo. As shown in Fig. 8, we locate V2279 Cyg in the diagram of L_X/L_{bol} as a function of the rotation period and compare it with the PMS stars in the

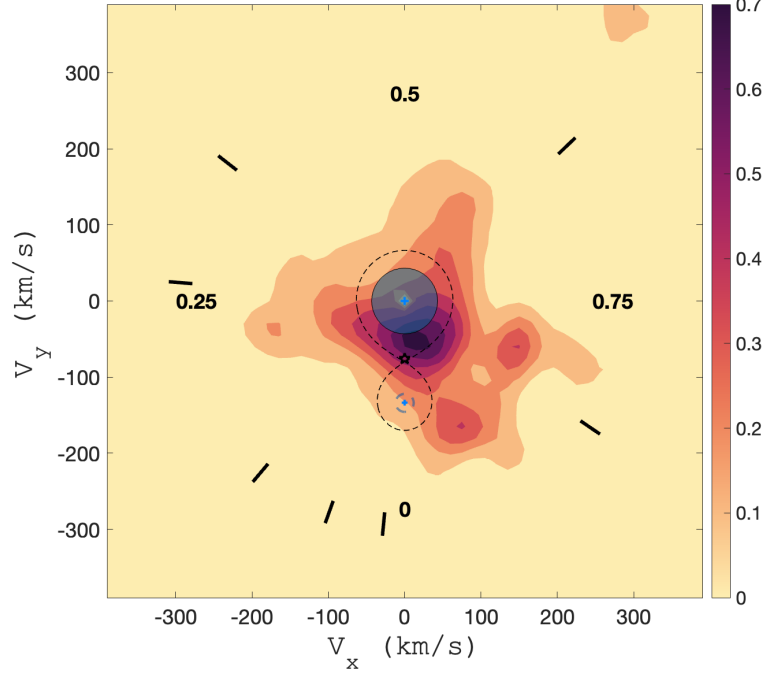


Figure 7. Prominence map (2020). The positions and relative sizes of the primary and secondary stars are marked with filled and dotted blue circles. The dotted black lines indicate the Roche lobe. The short black lines mark the observation phases. The color scale represents the local $H\alpha$ equivalent width, in units of picometers per 15 km s^{-1} square pixel.

young cluster h Persei ($\sim 13 \text{ Myr}$ old) (Argiroffi et al. 2016). Both measurements from Swift-XRT and XMM-Newton show that V2279 Cyg also lies in the so-called saturation region.

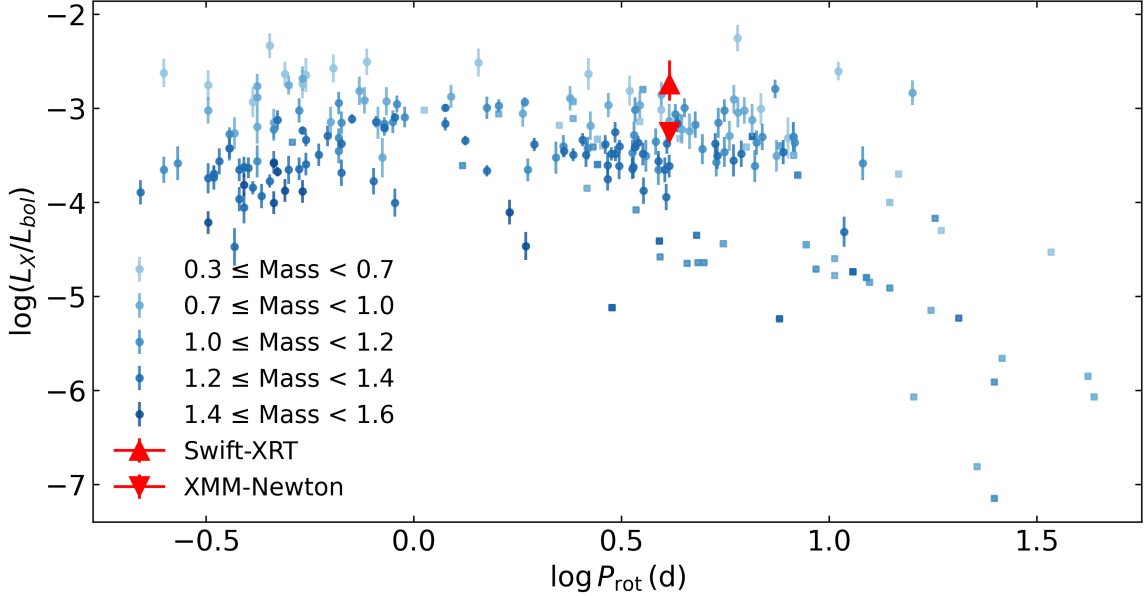


Figure 8. The logarithmic fractional X-ray luminosity $\log(L_X/L_{bol})$ vs. rotational period for V2279 Cyg, comparing with h Per members (circles) of different mass (Argiroffi et al. 2016), and MS stars (squares) in the unsaturated and saturated regime from Vidotto et al. (2014). The flat region on the left with a small period indicates a saturated regime of stellar dynamo. The X-ray emission of V2279 Cyg almost reaches the upper limit of saturated stars.

5.2. Active and inactive longitudes

The light curve analysis of V2279 Cyg reveals a consistent brightness minimum at $\phi \approx 0.5$, corresponding to a large star spot region around far-side hemisphere that persists across both *Kepler* and *TESS* observations, suggesting a tidally stabilized active longitude, which is also identified in other active binary systems (e.g., Jetsu 1996; Oláh 2006; Özdarcın et al. 2016). This phenomenon can be attributed to the constraint of the flux tubes under the influence of tidal effects (Holzwarth & Schüssler 2003a,b; Berdyugina 2005), with relatively weak differential rotation (Moss et al. 1995). The absence of flares around $\phi = 0.60$ to 0.78 during the *Kepler* observations indicates an inactive longitude of flare in this region. Assuming the inclination of 75° , the active region of the flare region can be roughly constrained in a small circle around latitude 71° and $\phi \sim 0.2$, with a radius of a few degrees. This area does not show a significant connection to the spotted region, differing from single stars, where flares typically occur at the same longitudes as the most spotted regions (e.g., the Sun Sammis et al. 2000 and wTTs Fernández et al. 2004). The inactive longitudes of flares in V2279 Cyg are likely due to the magnetic structure being limited by the binary nature, which is similar to the active longitude. On the other hand, the superflare found in the *TESS* observation suggests a different activity level from the time during *Kepler* observation, leading to a higher occurrence rate of flares in *TESS* observations as shown in the corresponding cumulative flare frequency distribution (FFD) shown in Fig. 13. Since the number of flares is still small for a solid statistic, more observations would help to investigate the active longitude of V2279 Cyg.

As a PMS, V2279 Cyg is expected to have a deep convective envelope or even be fully convective, similar to M-dwarfs. A recent study on the fully convective M-dwarf close binary CM Dra (Martin et al. 2024) reported no preference for orbital phase. Similarly, well-studied PMS binary system DQ Tau (Kóspál et al. 2018), with a rotation period of about 16 days, also shows no preferences for flare events. The inactive longitudes appear in V2279 Cyg at $\phi \sim 0.7$, yet the star's large inclination suggests that orbital motion is unlikely to be the main source of any obstruction. Meanwhile, DQ Tau also has a large inclination with a relatively stable light curve shape that can be described by a two-spot model. However, the mass ratio (DQ Tau $q = 0.93$) and orbital period could generate different tidal effects, thereby influencing the star's magnetic structure and flare-driving mechanism. On the other hand, the gap of normal flares shares almost the same phase as the only observed superflare, which released energy comparable to the sum of energy of other flares in one year. This coincidence may be connected to the star's magnetic structure. A detailed topology analysis (e.g., Zeeman Doppler imaging), would help clarify the role of magnetic geometry in modulating flare activity in V2279 Cyg.

5.3. Slingshot prominences as a source of stellar wind?

The prominences map is based on a minimum model to trace the emitting clouds co-rotating with the system. Our result showed that the emitting material concentrate opposite to the latitude of the spotted region, between the two components of the binary system, similar to the prominence structure to the active binary V471 Tau (Zaire et al. 2022). The failure of the fitting is likely to be caused by the heating of chromospheric activity or rapid evolution of prominences (Cang et al. 2021). At around $\phi \sim 0.4$ in 2018 and $\phi \sim 0.4$ & 0.5 in 2019, as shown in Fig. 16, the three enhanced emissions also happened around the most spotted region ($\phi = 0.5$), indicating that the heating process likely happened in the same area as spotted region, in agreement with the strong correlation between the EW and flux variation. On the other hand, the red-asymmetric structure of the emission profile suggests that the heated materials move away from the line-of-sight. Regarding that at this time, the spotted region is more or less facing us (Fig. 4), this scenario can be explained by the return of hot matter to the stellar surface, or corona rain (Daley-Yates et al. 2023).

The presence of superflares also reflects the confinement of a large amount of material by strong magnetic fields (e.g., Kowalski 2024), which could serve as a potential source of stellar winds (Vidotto 2021). As the $H\alpha$ lines are fully emitting during our observations, we estimated the mass of emitting materials stored around V2279 Cyg using the method based on Steeghs et al. (1996). We used the median value of the $H\alpha$ EWs from the LAMOST spectra and subtracted the EW measured from the synthetic spectrum as used in Fig. 14. We obtained a number density of hydrogen atoms of $\approx 3.9 \times 10^{15} \text{ m}^{-3}$, and the total mass of prominences is $\approx 6.8 \times 10^{18} \text{ kg}$ ($\sim 3.4 \times 10^{-12} M_\odot$). An enhanced $H\alpha$ emission event was observed on May 31, 2018, during which the EW increased by 3Å in 1 day. With the difference of mass, we can roughly estimate the mass loss as $\Delta M \approx 3.2 \times 10^{18} \text{ kg}$ ($\sim 1.6 \times 10^{-12} M_\odot$). Considering that there are over 10 flares observed by *Kepler* per year, the mass-loss through prominences eruptions can reach the order of $10^{19} \text{ kg yr}^{-1}$.

We also obtained the X-ray flux F_X of $6.7_{-2.7}^{+3.9} \times 10^{-13} \text{ erg s}^{-1} \text{ cm}^{-2}$ and $2.05_{-0.15}^{+0.15} \times 10^{-13} \text{ erg s}^{-1} \text{ cm}^{-2}$ from Swift-XRT (Evans et al. 2020, 2SXPS J191854.5+434923) and XMM-Newton (Jansen et al. 2001, 4XMM J191854.5+434925), respectively. Using the average X-ray luminosity of $2.5 \times 10^{31} \text{ erg s}^{-1}$, the surface X-ray flux is $F_{X*} \approx 3 \times 10^7 \text{ erg s}^{-1} \text{ cm}^{-2}$, corresponding to a coronal temperature of $\approx 9 \text{ MK}$ applying the relationship from Johnstone & Güdel (2015). Taking the solar mass-loss rate of $\dot{M}_\odot = 2 \times 10^{-14} M_\odot \text{ yr}^{-1}$, we estimated a stellar mass-loss rate of $\dot{M}_* \sim 583 \dot{M}_\odot$ according to See et al. (2017), which is about $2.3 \times 10^{19} \text{ kg yr}^{-1}$. This value is in agreement with our mass-loss estimation from the prominences, indicating that prominences contribute significantly to the stellar wind of V2279 Cyg, as other active young stars (Vaugh et al. 2021).

6. CONCLUSION

In this study, we have investigated the magnetic activity and longitudinal preferences of the pre-main sequence binary system V2279 Cyg using extensive photometric data from *Kepler* and *TESS*, combined with spectroscopic observations from LAMOST. Our analysis reveals that V2279 Cyg is a synchronized, nearly circular orbit binary with primary and secondary masses of approximately $0.86 M_\odot$ and $0.27 M_\odot$, respectively. The consistent clustering of large star spot regions near the far-side hemisphere across multiple observational epochs indicates the presence of a tidally stabilized active longitude on the primary star. Concurrently, we have identified an inactive longitude region where flare activity is notably absent during the *Kepler* observation, marking a novel discovery in the context of PMS binaries. The detection of a rare white light superflare, with an energy release of $2.5 \times 10^{37} \text{ erg}$, underscores the system's extreme magnetic activity. Additionally, our estimates of mass loss through slingshot prominences, corroborated by X-ray flux measurements, suggest that such prominences play a significant role in contributing to the stellar wind of V2279 Cyg. These findings provide valuable insights into the magnetic field geometry and dynamo processes in young binary systems, highlighting the crucial influence of tidal interactions in shaping both active and inactive longitudinal regions. Future studies, including detailed magnetic field mapping and continued monitoring of flare activities, will further illuminate the complex magnetic interactions and evolutionary dynamics governing pre-main-sequence binaries like V2279 Cyg.

TC is supported by the LAMOST fellowship as a Youth Researcher, which is supported by the Special Funding for Advanced Users, budgeted and administrated by the Center for Astronomical Mega-Science, Chinese Academy of Sciences (CAMS), and acknowledges funding from the China Postdoctoral Science Foundation (2023M730297). TC acknowledges funding from the support of the National Natural Science Foundation of China (NSFC) through grant 12273002. JNF acknowledges funding from the support of NSFC through grants 12090040/12090042/12427804. This work is supported by the China Manned Space Program with grant No. CMS-CSST-2025-A013, and the Central Guidance for Local Science and Technology Development Fund under No. ZYD2025QY27. JXW acknowledges the support of NSFC through grants 12203010, and the Natural Science Foundation of Chongqing (CQCSTC) under grants No. CSTB2023NSCQ-MSX1048. YY acknowledges funding from the support of NSFC through 12403101. This research has made use of the VizieR catalogue access tool, CDS, Strasbourg, France (Ochsenbein 1996). The original description of the VizieR service was published in Ochsenbein et al. (2000). Finally, We thank the reviewer for valuable comments and suggestions on this manuscript.

Facilities: *Kepler*, *TESS*, LAMOST, Swift-XRT, XMM-Newton

Software: astropy (Astropy Collaboration et al. 2013, 2018, 2022), laspec (Zhang et al. 2021), LSDpy: The GitHub repository for LSDpy is available at folsomcp/LSDpy.

APPENDIX

A. TIME-FREQUENCY ANALYSIS

We obtained *Kepler* long-cadence light curves Quarter 0-17 and extracted periods of 4.13 and 2.06 days using the Lomb-Scargle method ($S/N > 100$) (Fig. 9). To analyze the stability of the primary period, we performed a time-frequency analysis on *Kepler* data and found the primary period to be relatively stable in the 4-year observations with $P_{\text{rot}} = 4.1264 \pm 0.0001$ days (Fig. 10). The uncertainty is taken from the standard deviation from sLSP.

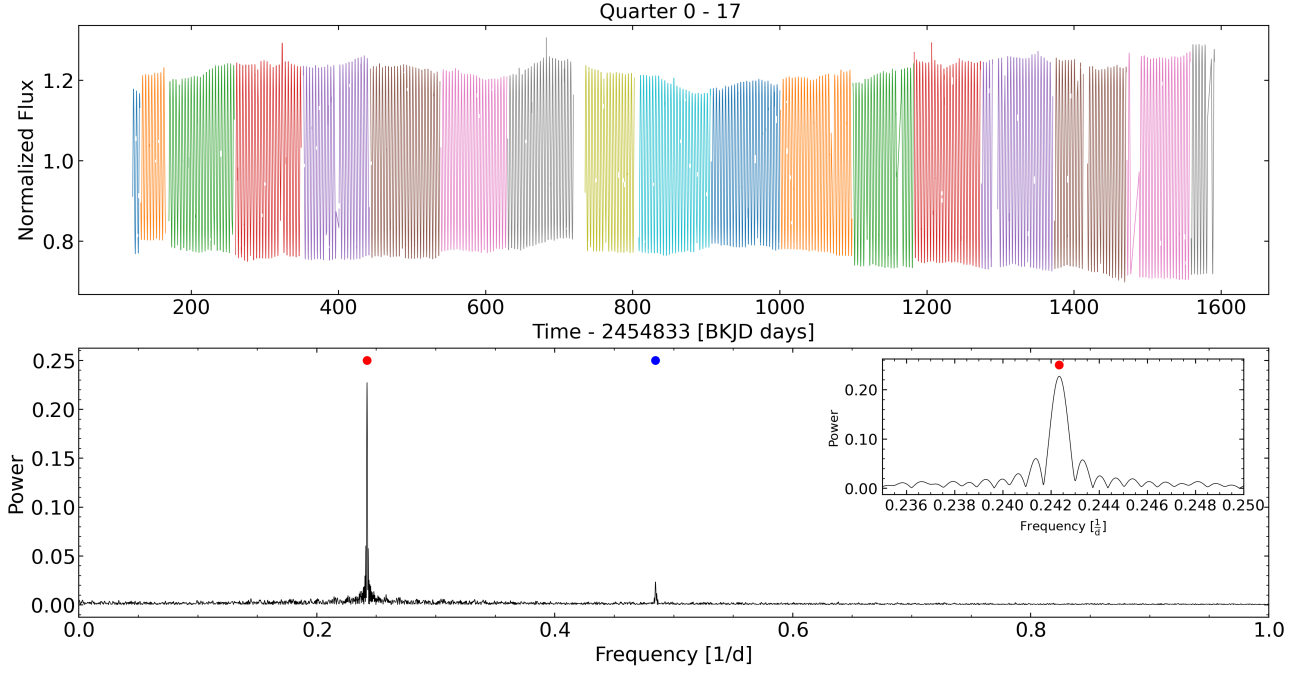


Figure 9. *Kepler* LC light curve (upper) and its power spectrum (lower). The red dot in the lower panel marks the main frequency and the blue dot marks its harmonic.

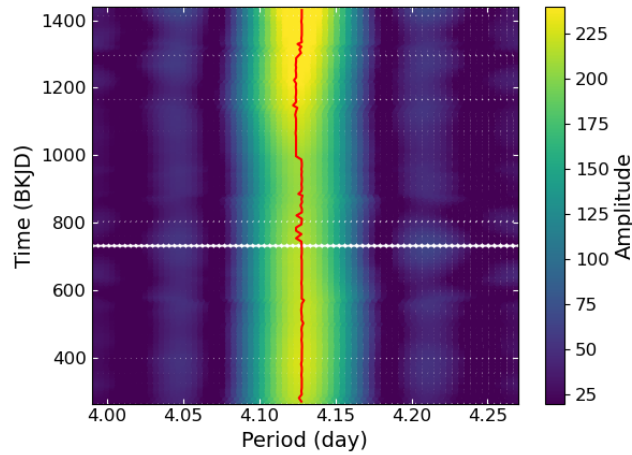


Figure 10. Sliding Lomb-Scargle periodogram (sLSP) for the *Kepler* LC light curve. The red line marks the maximum frequency value.

B. RADIAL VELOCITIES AND EWS

Table 2 lists the radial velocities of V2279 Cyg measured from both red- and blue-arm spectra of LAMOST MRS, derived with `laspec`, and EWs from $H\alpha$.

Table 3. The radial velocities of V2279 Cyg measured from the red- and blue-arm spectra of LAMOST medium-resolution survey. (Column 1 is the BJD time, Column 2 is the corresponding phase, and Columns 3 and 5 are RVs from LAMOST red- and blue-arm, respectively. Columns 4 and 6 are the corresponding errors. Column 7 lists the EWs.)

BJD (day)	Phase	RV _r (km/s)	err _r (km/s)	RV _b (km/s)	err _b (km/s)	EW (Å)
2458263.27	0.778	7.56	0.57	4.14	0.45	1.396
2458263.28	0.781	8.52	0.53	4.71	0.25	1.430
2458263.30	0.784	9.77	0.83	5.39	0.36	1.438
2458263.31	0.787	9.69	1.07	3.78	0.51	1.392
2458263.32	0.790	7.28	0.82	5.57	0.49	1.345
2458267.23	0.736	0.86	0.51	-4.75	0.36	2.274
2458267.24	0.739	0.02	0.66	-3.75	0.34	2.173
2458267.25	0.743	0.12	0.52	-4.45	0.31	2.103
2458267.26	0.746	4.91	0.52	-3.45	0.32	2.041
2458267.28	0.749	1.61	0.81	-3.55	0.18	1.973
2458267.29	0.752	1.78	0.66	-2.93	0.30	1.960
2458267.31	0.757	2.27	0.65	-2.40	0.26	1.901
2458268.24	0.981	-25.96	0.84	-29.85	0.37	0.770
2458268.25	0.983	-25.75	0.37	-31.31	0.27	0.772
2458268.25	0.985	-26.87	0.76	-31.71	0.25	0.791
2458268.26	0.988	-27.21	0.44	-32.71	0.40	0.757
2458268.27	0.990	-27.75	0.64	-32.65	0.30	0.708
2458268.28	0.992	-28.41	0.66	-32.60	0.32	0.750
2458268.29	0.995	-28.41	0.90	-33.50	0.44	0.704
2458268.30	0.997	-29.72	0.74	-33.62	0.38	0.723
2458268.31	0.000	-30.00	0.95	-34.72	0.34	0.730
2458269.25	0.227	-63.08	0.36	-67.38	0.19	1.268
2458269.26	0.230	-64.53	0.46	-66.58	0.17	1.325
2458269.28	0.234	-62.92	0.28	-66.97	0.20	1.280
2458269.29	0.237	-64.67	0.80	-66.78	0.34	1.223
2458269.30	0.240	-63.19	0.37	-67.07	0.24	1.278
2458270.25	0.470	-36.65	2.62	-40.28	0.99	4.435
2458270.27	0.474	-37.53	2.17	-38.30	1.00	4.622
2458270.29	0.478	-39.02	2.55	-38.73	1.83	4.812
2458270.30	0.482	-32.53	2.59	-36.59	1.50	4.484
2458625.27	0.507	-24.35	1.02	-28.18	0.55	2.736
2458625.29	0.511	-25.60	1.36	-29.57	0.60	2.599
2458644.23	0.100	-40.71	0.62	-45.00	0.19	1.145
2458644.24	0.104	-43.82	0.52	-47.91	0.16	1.111
2458644.26	0.108	-43.44	0.46	-49.79	0.21	1.143
2458644.27	0.112	-46.70	0.79	-51.73	0.15	1.139
2458646.24	0.590	-13.91	0.91	-13.60	0.34	3.514
2458646.26	0.594	-13.99	0.76	-12.81	0.32	3.359
2458646.28	0.599	-12.58	1.06	-11.28	0.28	3.280

BJD (day)	Phase	RV_r (km/s)	err_r (km/s)	RV_b (km/s)	err_b (km/s)	EW (Å)
2459001.23	0.618	-4.74	1.44	-5.85	0.41	1.908
2459001.25	0.625	-2.48	0.52	-4.48	0.18	1.788
2459001.27	0.629	-1.39	0.41	-3.40	0.17	1.764
2459001.29	0.633	-1.79	0.61	-2.95	0.24	1.803
2459001.30	0.637	-3.31	1.10	-3.38	0.58	1.753
2459003.22	0.101	-49.01	0.72	-49.98	0.31	0.917
2459003.24	0.105	-50.00	0.56	-50.41	0.28	0.986
2459003.25	0.109	-51.47	0.48	-51.36	0.25	1.036
2459003.27	0.113	-53.82	0.59	-52.70	0.24	1.041
2459003.28	0.117	-54.76	0.58	-52.69	0.29	1.076
2459003.30	0.121	-55.92	0.57	-54.28	0.20	1.115
2459004.24	0.348	-50.98	0.55	-51.37	0.23	2.151
2459004.25	0.352	-48.99	0.39	-50.45	0.18	2.181
2459004.27	0.356	-49.32	0.52	-50.42	0.19	2.278
2459004.29	0.360	-49.57	0.48	-49.75	0.26	2.287
2459004.30	0.363	-48.69	0.54	-49.35	0.29	2.246
2459006.29	0.845	4.41	0.57	4.14	0.20	1.147
2459011.26	0.048	-34.34	0.58	-34.28	0.34	1.686
2459011.27	0.052	-34.75	0.91	-35.92	0.27	2.194
2459011.29	0.056	-37.30	0.94	-37.64	0.61	2.304
2459011.30	0.060	-38.18	0.94	-38.57	0.66	2.641
2459015.20	0.004	-27.25	0.29	-26.35	0.11	0.958
2459015.22	0.008	-27.55	0.31	-27.33	0.14	1.035
2459015.23	0.012	-28.89	0.31	-28.51	0.14	1.013
2459015.25	0.018	-29.54	0.41	-30.02	0.17	0.988
2459015.27	0.022	-31.01	0.32	-31.16	0.16	1.005
2459015.29	0.026	-31.88	0.61	-31.99	0.14	1.016
2459016.24	0.257	-59.67	0.43	-58.18	0.19	2.378
2459016.26	0.261	-58.91	0.75	-57.85	0.20	2.364
2459016.27	0.265	-57.68	0.98	-58.20	0.26	2.288
2459016.29	0.269	-59.35	0.83	-57.62	0.24	2.334

C. MARKOV CHAIN MONTE CARLO SAMPLING FOR SPOT MODELING

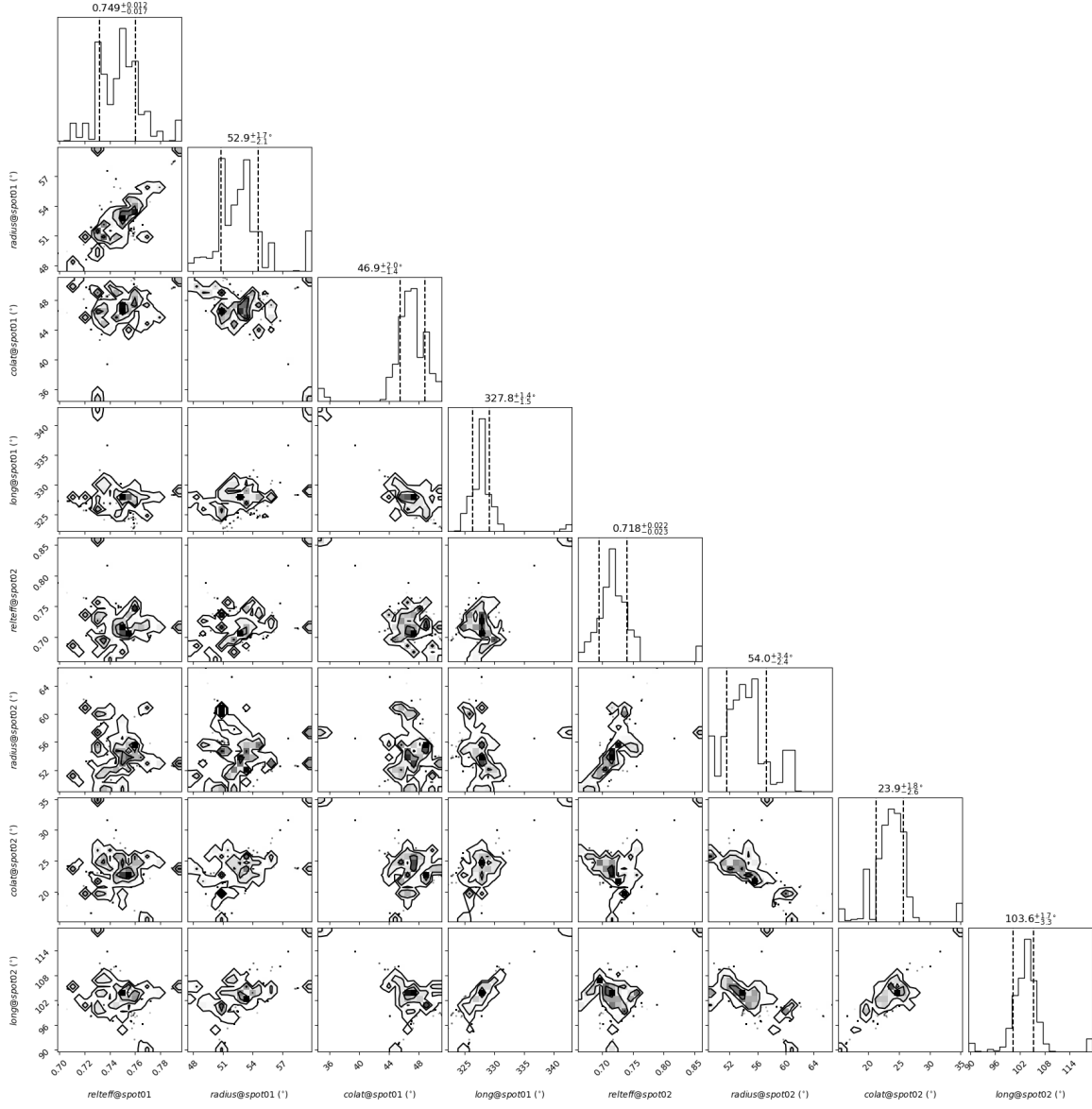


Figure 11. Corner map of the MCMC fitting result. The dashed lines show the 1σ edges of the MCMC results.

D. FLARE ENERGIES

We investigated the flare frequency distribution (FFD) using the cumulative FFD formalism (Lacy et al. 1976; Xing et al. 2024), expressed as:

$$\log(\nu) = \beta + (1 - \alpha)\log(E), \quad (\text{D1})$$

where ν is the number of flares per year with an energy above a specific threshold, and E represents the energy of the flares. The phase-folded distribution of flare energies is presented in Fig. 5, and the corresponding cumulative FFD is shown in Fig. 13. The fitted α for V2279 Cyg is 1.54 ± 0.2 for both *Kepler* and *TESS*, which is similar to the $\alpha = 1.52$ for PMS binary DQ Tau (Kóspál et al. 2018).

Table 4. The energies of flares in *TESS*

Time_Start (BKJD)	Time_Stop (BKJD)	E_{flare} (erg)	Sector
3854.572184	3855.280526	2.53E+37	14
3860.738926	3860.947262	4.51E+35	14
4573.874051	4573.943496	8.87E+34	40
4574.401833	4574.575446	1.43E+35	40
4594.929678	4595.138011	6.41E+35	41
4604.089338	4604.242114	2.47E+35	41
4954.519795	4954.867017	9.49E+35	54
5488.110207	5488.161133	8.72E+34	74
5501.994595	5502.119598	2.42E+35	74
5528.301021	5528.395933	3.29E+35	75

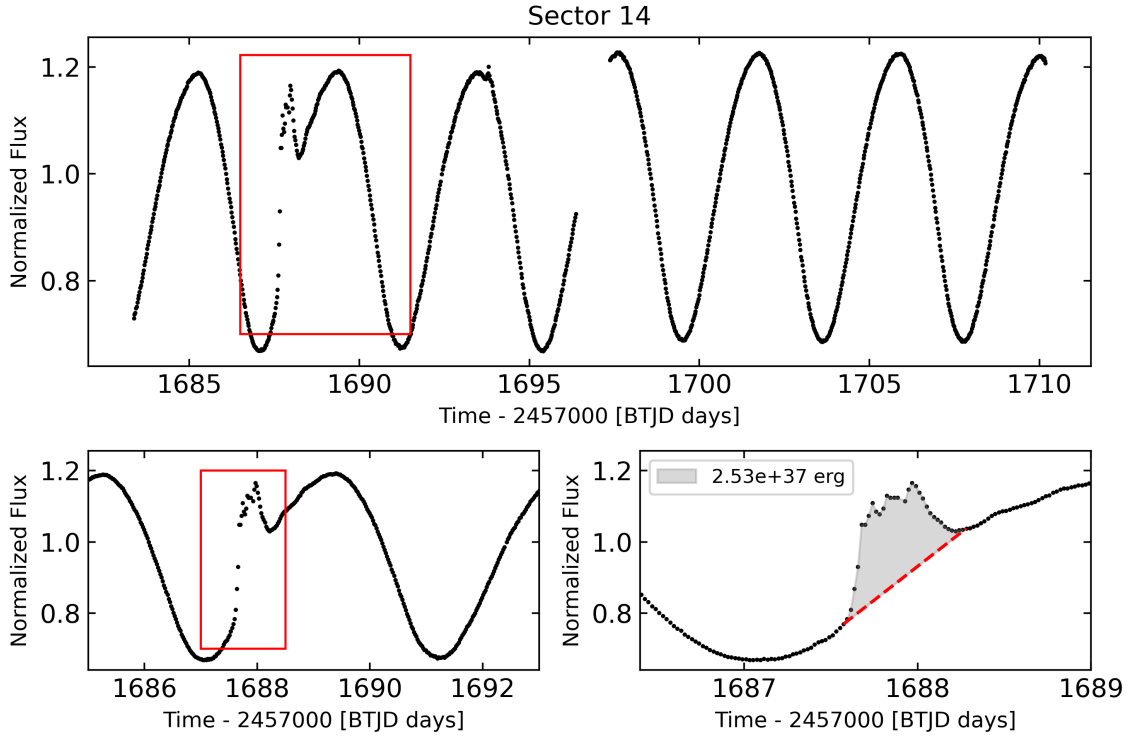


Figure 12. The superflare in *TESS* Sector 14.

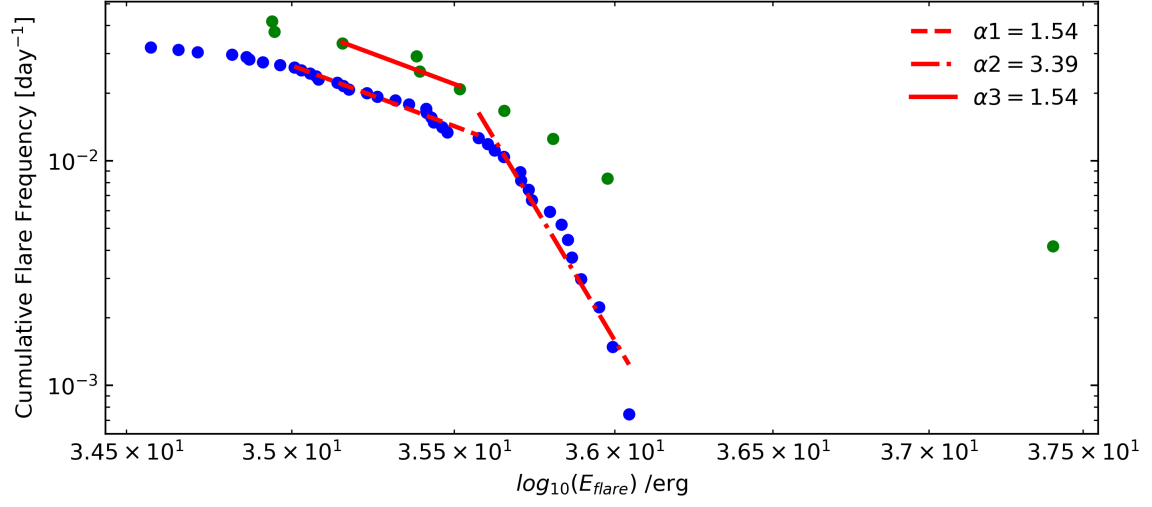


Figure 13. The corresponding cumulative flare frequency distribution (FFD) of *Kepler* (blue) and *TESS* (green) flares. The α parameters of Eq.D1 fitting are shown with red lines.

E. SED

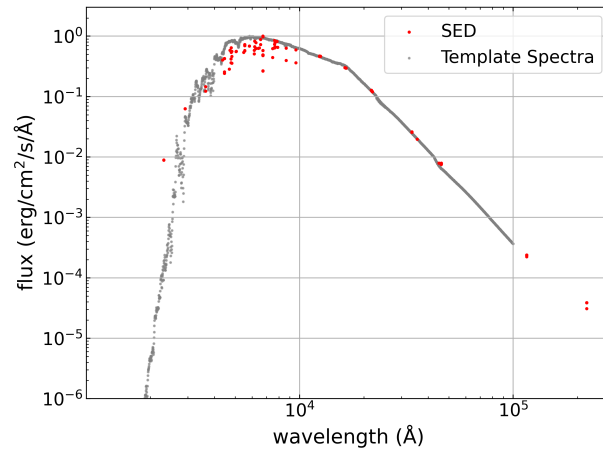


Figure 14. SED of V2279 Cyg. The template spectra is from [Coelho \(2014\)](#), with $T_{\text{eff}} = 4500 \text{ K}$, $\log g = 3$, $[\text{Fe}/\text{H}] = -0.5$, $[\alpha/\text{Fe}] = 0$. The SED data were from VizieR ([Ochsenbein 1996](#)).

F. LSD AND H-ALPHA PROFILES

To enhance the S/N of LAMOST spectra, we applied the LSD technique, and the resulting profiles are presented in Fig. 15. Variations induced by stellar spots are detectable. Additionally, the original spectra reveal prominent H α emissions, which exhibit temporal variability (Fig. 16).

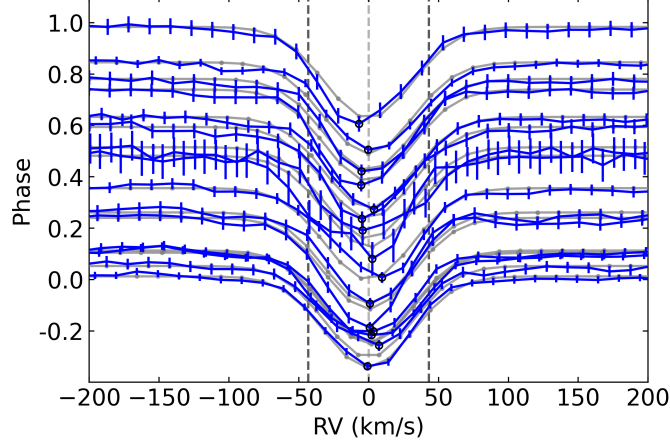


Figure 15. LSD profiles (blue lines with error bars) arranged by phase, spanning from 2018 to 2020. The gray lines represent the mean photospheric structures modeled using Gaussian profiles. Black circles indicate the minimum value of each profile. The vertical black dashed lines mark the $\pm v \sin i$.

REFERENCES

- Akerlof, C., Amrose, S., Balsano, R., et al. 2000, *AJ*, 119, 1901, doi: [10.1086/301321](https://doi.org/10.1086/301321)
- Akeson, R. L., Jensen, E. L., Carpenter, J., et al. 2019, *The Astrophysical Journal*, 872, 158
- Argiroffi, C., Caramazza, M., Micela, G., et al. 2016, *A&A*, 589, A113, doi: [10.1051/0004-6361/201526539](https://doi.org/10.1051/0004-6361/201526539)
- Astropy Collaboration, Robitaille, T. P., Tollerud, E. J., et al. 2013, *A&A*, 558, A33, doi: [10.1051/0004-6361/201322068](https://doi.org/10.1051/0004-6361/201322068)
- Astropy Collaboration, Price-Whelan, A. M., Sipőcz, B. M., et al. 2018, *AJ*, 156, 123, doi: [10.3847/1538-3881/aabc4f](https://doi.org/10.3847/1538-3881/aabc4f)
- Astropy Collaboration, Price-Whelan, A. M., Lim, P. L., et al. 2022, *ApJ*, 935, 167, doi: [10.3847/1538-4357/ac7c74](https://doi.org/10.3847/1538-4357/ac7c74)
- Berdyugina, S. V. 2005, *Living Reviews in Solar Physics*, 2, 8, doi: [10.12942/lrsp-2005-8](https://doi.org/10.12942/lrsp-2005-8)
- Berdyugina, S. V., Jankov, S., Ilyin, I., Tuominen, I., & Fekel, F. C. 1998, *A&A*, 334, 863
- Berger, T. A., Huber, D., van Saders, J. L., et al. 2020, *AJ*, 159, 280, doi: [10.3847/1538-3881/159/6/280](https://doi.org/10.3847/1538-3881/159/6/280)
- Cang, T. Q., Petit, P., Donati, J. F., & Folsom, C. P. 2021, *A&A*, 654, A42, doi: [10.1051/0004-6361/202141975](https://doi.org/10.1051/0004-6361/202141975)
- Cang, T. Q., Petit, P., Donati, J. F., et al. 2020, *A&A*, 643, A39, doi: [10.1051/0004-6361/202037693](https://doi.org/10.1051/0004-6361/202037693)
- Carroll, T. A., Strassmeier, K. G., Rice, J. B., & Küstler, A. 2012, *A&A*, 548, A95, doi: [10.1051/0004-6361/201220215](https://doi.org/10.1051/0004-6361/201220215)
- Choi, J., Dotter, A., Conroy, C., et al. 2016, *ApJ*, 823, 102, doi: [10.3847/0004-637X/823/2/102](https://doi.org/10.3847/0004-637X/823/2/102)
- Coelho, P. R. T. 2014, *MNRAS*, 440, 1027, doi: [10.1093/mnras/stu365](https://doi.org/10.1093/mnras/stu365)
- Collier Cameron, A. 1996, in *IAU Symposium*, Vol. 176, *Stellar Surface Structure*, ed. K. G. Strassmeier & J. L. Linsky, 449
- Conroy, K. E., Kochoska, A., Hey, D., et al. 2020, *ApJS*, 250, 34, doi: [10.3847/1538-4365/abb4e2](https://doi.org/10.3847/1538-4365/abb4e2)
- Creevey, O. L., Sordo, R., Pailler, F., et al. 2023, *A&A*, 674, A26, doi: [10.1051/0004-6361/202243688](https://doi.org/10.1051/0004-6361/202243688)
- Dahlmark, L. 2000, *Information Bulletin on Variable Stars*, 4898, 1
- Daley-Yates, S., Jardine, M. M., & Johnston, C. D. 2023, *MNRAS*, 526, 1646, doi: [10.1093/mnras/stad2752](https://doi.org/10.1093/mnras/stad2752)
- De Cat, P., Fu, J. N., Ren, A. B., et al. 2015, *ApJS*, 220, 19, doi: [10.1088/0067-0049/220/1/19](https://doi.org/10.1088/0067-0049/220/1/19)
- Dharmawardena, T. E., Bailer-Jones, C. A. L., Fousneau, M., et al. 2024, *MNRAS*, doi: [10.1093/mnras/stae1474](https://doi.org/10.1093/mnras/stae1474)
- Donati, J. F., Mengel, M., Carter, B. D., et al. 2000, *MNRAS*, 316, 699, doi: [10.1046/j.1365-8711.2000.03570.x](https://doi.org/10.1046/j.1365-8711.2000.03570.x)

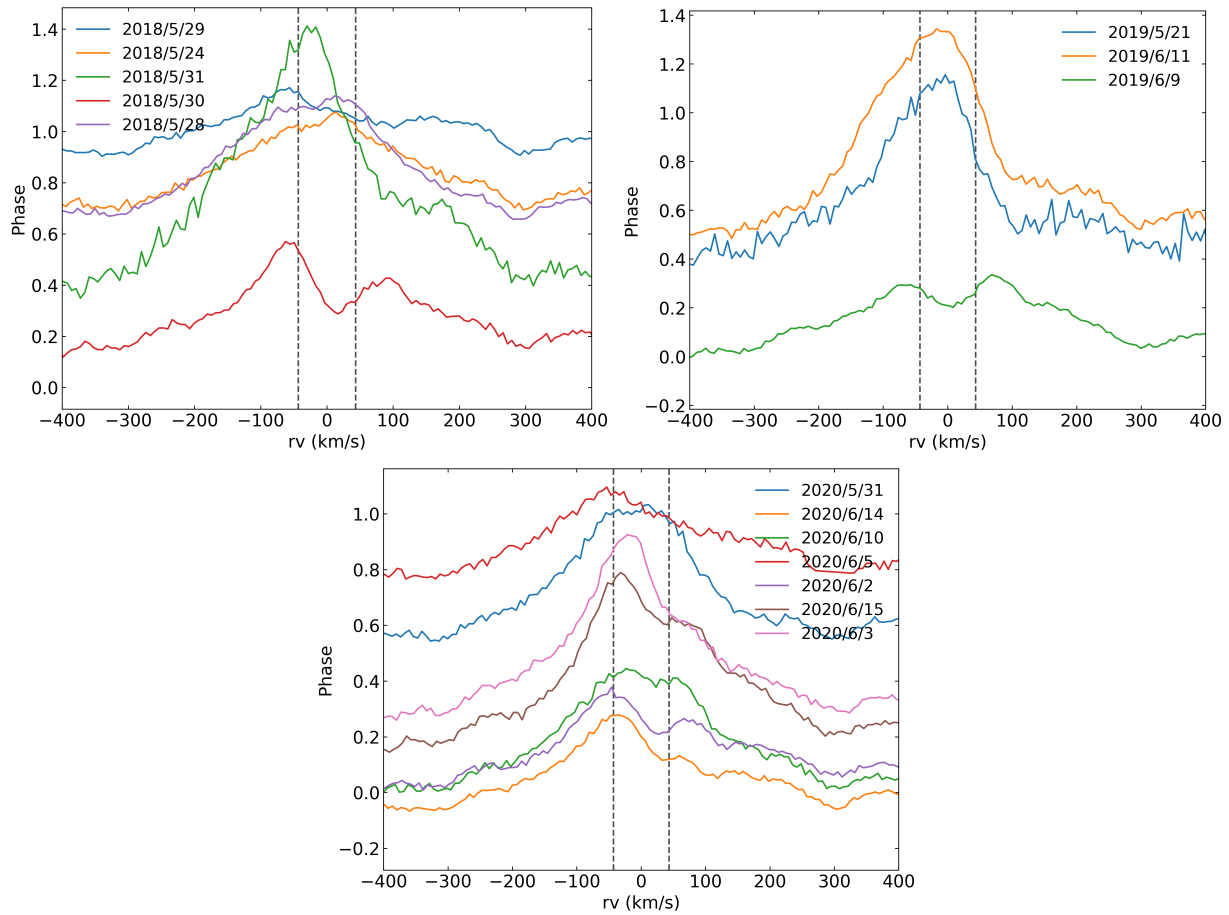


Figure 16. $H\alpha$ profiles averaged over individual nights during 2018–2020 (from left to right), after correcting the RV caused by the binary system. $\text{BJD}_0 = 2458268.3132$ was chosen as the initial time for phase-folding. Two vertical dashed lines show the $\pm v \sin i$ (Frasca et al. 2022).

Donati, J. F., Semel, M., Carter, B. D., Rees, D. E., & Collier Cameron, A. 1997, *MNRAS*, 291, 658, doi: [10.1093/mnras/291.4.658](https://doi.org/10.1093/mnras/291.4.658)

Donati, J. F., Hébrard, E., Hussain, G. A. J., et al. 2015, *MNRAS*, 453, 3706, doi: [10.1093/mnras/stv1837](https://doi.org/10.1093/mnras/stv1837)

Dotter, A. 2016, *ApJS*, 222, 8, doi: [10.3847/0067-0049/222/1/8](https://doi.org/10.3847/0067-0049/222/1/8)

Evans, P. A., Page, K. L., Osborne, J. P., et al. 2020, *ApJS*, 247, 54, doi: [10.3847/1538-4365/ab7db9](https://doi.org/10.3847/1538-4365/ab7db9)

Fernández, M., Stelzer, B., Henden, A., et al. 2004, *A&A*, 427, 263, doi: [10.1051/0004-6361:20034463](https://doi.org/10.1051/0004-6361:20034463)

Finocietty, B., Donati, J. F., Grankin, K., et al. 2023, *MNRAS*, 520, 3049, doi: [10.1093/mnras/stad267](https://doi.org/10.1093/mnras/stad267)

Fleming, D. P., Barnes, R., Davenport, J. R. A., & Luger, R. 2019, *ApJ*, 881, 88, doi: [10.3847/1538-4357/ab2ed2](https://doi.org/10.3847/1538-4357/ab2ed2)

Folsom, C. P., Bouvier, J., Petit, P., et al. 2018, *MNRAS*, 474, 4956, doi: [10.1093/mnras/stx3021](https://doi.org/10.1093/mnras/stx3021)

Foreman-Mackey, D., Hogg, D. W., Lang, D., & Goodman, J. 2013, *PASP*, 125, 306, doi: [10.1086/670067](https://doi.org/10.1086/670067)

Frasca, A., Molenda-Żakowicz, J., De Cat, P., et al. 2016, *A&A*, 594, A39, doi: [10.1051/0004-6361/201628337](https://doi.org/10.1051/0004-6361/201628337)

Frasca, A., Molenda-Żakowicz, J., Alonso-Santiago, J., et al. 2022, *A&A*, 664, A78, doi: [10.1051/0004-6361/202243268](https://doi.org/10.1051/0004-6361/202243268)

Fu, J.-N., Cat, P. D., Zong, W., et al. 2020, *Research in Astronomy and Astrophysics*, 20, 167, doi: [10.1088/1674-4527/20/10/167](https://doi.org/10.1088/1674-4527/20/10/167)

Gaia Collaboration. 2020, *VizieR Online Data Catalog: Gaia EDR3* (Gaia Collaboration, 2020), *VizieR On-line Data Catalog: I/350*. Originally published in: 2021A&A...649A...1G; doi: [10.5270/esa-lug](https://doi.org/10.5270/esa-lug), doi: [10.26093/cds/vizier.1350](https://doi.org/10.26093/cds/vizier.1350)

Gallet, F., & Bouvier, J. 2013, *A&A*, 556, A36, doi: [10.1051/0004-6361/201321302](https://doi.org/10.1051/0004-6361/201321302)

Gallet, F., Charbonnel, C., Amard, L., et al. 2017, *A&A*, 597, A14, doi: [10.1051/0004-6361/201629034](https://doi.org/10.1051/0004-6361/201629034)

Guerrero, G., Zaire, B., Smolarkiewicz, P. K., et al. 2019, *ApJ*, 880, 6, doi: [10.3847/1538-4357/ab224a](https://doi.org/10.3847/1538-4357/ab224a)

Gunn, A. G., Mitrou, C. K., & Doyle, J. G. 1998, *MNRAS*, 296, 150, doi: [10.1046/j.1365-8711.1998.01347.x](https://doi.org/10.1046/j.1365-8711.1998.01347.x)

- Gyenge, N., Ludmány, A., & Baranyi, T. 2016, *ApJ*, 818, 127, doi: [10.3847/0004-637X/818/2/127](https://doi.org/10.3847/0004-637X/818/2/127)
- Hill, C. A., Folsom, C. P., Donati, J. F., et al. 2019, *MNRAS*, 484, 5810, doi: [10.1093/mnras/stz403](https://doi.org/10.1093/mnras/stz403)
- Holzwarth, V., & Schüssler, M. 2003a, *A&A*, 405, 291, doi: [10.1051/0004-6361:20030582](https://doi.org/10.1051/0004-6361:20030582)
- . 2003b, *A&A*, 405, 303, doi: [10.1051/0004-6361:20030584](https://doi.org/10.1051/0004-6361:20030584)
- Horvat, M., Conroy, K. E., Pablo, H., et al. 2018, *ApJS*, 237, 26, doi: [10.3847/1538-4365/aacd0f](https://doi.org/10.3847/1538-4365/aacd0f)
- Huang, C. X., Vanderburg, A., Pál, A., et al. 2020a, *Research Notes of the American Astronomical Society*, 4, 204, doi: [10.3847/2515-5172/abca2e](https://doi.org/10.3847/2515-5172/abca2e)
- . 2020b, *Research Notes of the American Astronomical Society*, 4, 206, doi: [10.3847/2515-5172/abca2d](https://doi.org/10.3847/2515-5172/abca2d)
- Huang, L. C., Ip, W. H., Lin, C. L., et al. 2020c, *ApJ*, 892, 58, doi: [10.3847/1538-4357/ab774a](https://doi.org/10.3847/1538-4357/ab774a)
- Hussain, G. A. J., & Alecian, E. 2014, in *IAU Symposium*, Vol. 302, *Magnetic Fields throughout Stellar Evolution*, ed. P. Petit, M. Jardine, & H. C. Spruit, 25–37, doi: [10.1017/S1743921314001653](https://doi.org/10.1017/S1743921314001653)
- Jansen, F., Lumb, D., Altieri, B., et al. 2001, *A&A*, 365, L1, doi: [10.1051/0004-6361:20000036](https://doi.org/10.1051/0004-6361:20000036)
- Jeffers, S. V. 2005, *MNRAS*, 359, 729, doi: [10.1111/j.1365-2966.2005.08951.x](https://doi.org/10.1111/j.1365-2966.2005.08951.x)
- Jetsu, L. 1996, *A&A*, 314, 153
- Johnstone, C. P., & Güdel, M. 2015, *A&A*, 578, A129, doi: [10.1051/0004-6361/201425283](https://doi.org/10.1051/0004-6361/201425283)
- Johnstone, C. P., Pilat-Lohinger, E., Lüftinger, T., Güdel, M., & Stökl, A. 2019, *A&A*, 626, A22, doi: [10.1051/0004-6361/201832805](https://doi.org/10.1051/0004-6361/201832805)
- Jones, D., Conroy, K. E., Horvat, M., et al. 2020, *ApJS*, 247, 63, doi: [10.3847/1538-4365/ab7927](https://doi.org/10.3847/1538-4365/ab7927)
- Koch, D. G., Borucki, W. J., Basri, G., et al. 2010, *ApJL*, 713, L79, doi: [10.1088/2041-8205/713/2/L79](https://doi.org/10.1088/2041-8205/713/2/L79)
- Kóspál, Á., Ábrahám, P., Zsidi, G., et al. 2018, *ApJ*, 862, 44, doi: [10.3847/1538-4357/aacafa](https://doi.org/10.3847/1538-4357/aacafa)
- Kowalski, A. F. 2024, *Living Reviews in Solar Physics*, 21, 1, doi: [10.1007/s41116-024-00039-4](https://doi.org/10.1007/s41116-024-00039-4)
- Kunimoto, M., Tey, E., Fong, W., et al. 2022, *Research Notes of the American Astronomical Society*, 6, 236, doi: [10.3847/2515-5172/aca158](https://doi.org/10.3847/2515-5172/aca158)
- Kunimoto, M., Huang, C., Tey, E., et al. 2021, *Research Notes of the American Astronomical Society*, 5, 234, doi: [10.3847/2515-5172/ac2ef0](https://doi.org/10.3847/2515-5172/ac2ef0)
- Kupka, F., Piskunov, N., Ryabchikova, T. A., Stempels, H. C., & Weiss, W. W. 1999, *A&AS*, 138, 119, doi: [10.1051/aas:1999267](https://doi.org/10.1051/aas:1999267)
- Lacy, C. H., Moffett, T. J., & Evans, D. S. 1976, *ApJS*, 30, 85, doi: [10.1086/190358](https://doi.org/10.1086/190358)
- Lanza, A. F., Flaccomio, E., Messina, S., et al. 2016, *A&A*, 592, A140, doi: [10.1051/0004-6361/201628382](https://doi.org/10.1051/0004-6361/201628382)
- Leung, H. W., & Bovy, J. 2019, *MNRAS*, 483, 3255, doi: [10.1093/mnras/sty3217](https://doi.org/10.1093/mnras/sty3217)
- Li, J., & Chen, X. 2023, *Universe*, 9, 364, doi: [10.3390/universe9080364](https://doi.org/10.3390/universe9080364)
- Li, J., Tenenbaum, P., Twicken, J. D., et al. 2019, *PASP*, 131, 024506, doi: [10.1088/1538-3873/aaf44d](https://doi.org/10.1088/1538-3873/aaf44d)
- Maíz Apellániz, J. 2024, *arXiv e-prints*, arXiv:2401.01116, doi: [10.48550/arXiv.2401.01116](https://doi.org/10.48550/arXiv.2401.01116)
- Majewski, S. R., Schiavon, R. P., Frinchaboy, P. M., et al. 2017, *AJ*, 154, 94, doi: [10.3847/1538-3881/aa784d](https://doi.org/10.3847/1538-3881/aa784d)
- Mamajek, E. E., Torres, G., Prsa, A., et al. 2015, *arXiv e-prints*, arXiv:1510.06262, doi: [10.48550/arXiv.1510.06262](https://doi.org/10.48550/arXiv.1510.06262)
- Marsh, T. R., & Horne, K. 1988, *MNRAS*, 235, 269, doi: [10.1093/mnras/235.1.269](https://doi.org/10.1093/mnras/235.1.269)
- Martin, D. V., Sethi, R., Armitage, T., et al. 2024, *MNRAS*, 528, 963, doi: [10.1093/mnras/stae015](https://doi.org/10.1093/mnras/stae015)
- Mathieu, R. D. 1994, *ARA&A*, 32, 465, doi: [10.1146/annurev.aa.32.090194.002341](https://doi.org/10.1146/annurev.aa.32.090194.002341)
- Moss, D., Barker, D. M., Brandenburg, A., & Tuominen, I. 1995, *A&A*, 294, 155
- Moss, D., & Tuominen, I. 1997, *A&A*, 321, 151
- Nicholson, B. A., Hussain, G., Donati, J. F., et al. 2021, *MNRAS*, 504, 2461, doi: [10.1093/mnras/stab879](https://doi.org/10.1093/mnras/stab879)
- Nicholson, B. A., Hussain, G. A. J., Donati, J. F., et al. 2018, *MNRAS*, 480, 1754, doi: [10.1093/mnras/sty1965](https://doi.org/10.1093/mnras/sty1965)
- Ochsenbein, F. 1996, *The VizieR database of astronomical catalogues*, CDS, Centre de Données astronomiques de Strasbourg, doi: [10.26093/CDS/VIZIER](https://doi.org/10.26093/CDS/VIZIER)
- Ochsenbein, F., Bauer, P., & Marcout, J. 2000, *A&AS*, 143, 23, doi: [10.1051/aas:2000169](https://doi.org/10.1051/aas:2000169)
- Oláh, K. 2006, *Ap&SS*, 304, 145, doi: [10.1007/s10509-006-9096-x](https://doi.org/10.1007/s10509-006-9096-x)
- Oláh, K., Kővári, Z., Günther, M. N., et al. 2021, *A&A*, 647, A62, doi: [10.1051/0004-6361/202039674](https://doi.org/10.1051/0004-6361/202039674)
- Oláh, K., Seli, B., Kővári, Z., Kriskovics, L., & Vida, K. 2022, *A&A*, 668, A101, doi: [10.1051/0004-6361/202243789](https://doi.org/10.1051/0004-6361/202243789)
- Özdarcan, O., Carroll, T. A., Künstler, A., et al. 2016, *A&A*, 593, A123, doi: [10.1051/0004-6361/201628545](https://doi.org/10.1051/0004-6361/201628545)
- Paxton, B., Bildsten, L., Dotter, A., et al. 2011, *ApJS*, 192, 3, doi: [10.1088/0067-0049/192/1/3](https://doi.org/10.1088/0067-0049/192/1/3)
- Paxton, B., Cantiello, M., Arras, P., et al. 2013, *ApJS*, 208, 4, doi: [10.1088/0067-0049/208/1/4](https://doi.org/10.1088/0067-0049/208/1/4)
- Paxton, B., Marchant, P., Schwab, J., et al. 2015, *ApJS*, 220, 15, doi: [10.1088/0067-0049/220/1/15](https://doi.org/10.1088/0067-0049/220/1/15)

- Petit, P., Donati, J. F., Jardine, M., & Collier Cameron, A. 2005, in IAU Symposium, Vol. 226, Coronal and Stellar Mass Ejections, ed. K. Dere, J. Wang, & Y. Yan, 511–512, doi: [10.1017/S1743921305001158](https://doi.org/10.1017/S1743921305001158)
- Pigulski, A., Pojmański, G., Pilecki, B., & Szczygieł, D. M. 2009, *AcA*, 59, 33, doi: [10.48550/arXiv.0903.4921](https://doi.org/10.48550/arXiv.0903.4921)
- Piskunov, N. E., Kupka, F., Ryabchikova, T. A., Weiss, W. W., & Jeffery, C. S. 1995, *A&AS*, 112, 525
- Prša, A., & Zwitter, T. 2005, *ApJ*, 628, 426, doi: [10.1086/430591](https://doi.org/10.1086/430591)
- Prša, A., Conroy, K. E., Horvat, M., et al. 2016, *ApJS*, 227, 29, doi: [10.3847/1538-4365/227/2/29](https://doi.org/10.3847/1538-4365/227/2/29)
- Ricker, G. R., Winn, J. N., Vanderspek, R., et al. 2015, *Journal of Astronomical Telescopes, Instruments, and Systems*, 1, 014003, doi: [10.1117/1.JATIS.1.1.014003](https://doi.org/10.1117/1.JATIS.1.1.014003)
- Sammis, I., Tang, F., & Zirin, H. 2000, *ApJ*, 540, 583, doi: [10.1086/309303](https://doi.org/10.1086/309303)
- See, V., Jardine, M., Vidotto, A. A., et al. 2017, *MNRAS*, 466, 1542, doi: [10.1093/mnras/stw3094](https://doi.org/10.1093/mnras/stw3094)
- Sethi, R., & Martin, D. V. 2024, *MNRAS*, 529, 4442, doi: [10.1093/mnras/stae717](https://doi.org/10.1093/mnras/stae717)
- Simonian, G. V. A., Pinsonneault, M. H., & Terndrup, D. M. 2019, *ApJ*, 871, 174, doi: [10.3847/1538-4357/aaf97c](https://doi.org/10.3847/1538-4357/aaf97c)
- Skelly, M. B., Donati, J. F., Bouvier, J., et al. 2010, *MNRAS*, 403, 159, doi: [10.1111/j.1365-2966.2009.16132.x](https://doi.org/10.1111/j.1365-2966.2009.16132.x)
- Steeghs, D., Horne, K., Marsh, T. R., & Donati, J. F. 1996, *MNRAS*, 281, 626, doi: [10.1093/mnras/281.2.626](https://doi.org/10.1093/mnras/281.2.626)
- Szabó, R., Szabados, L., Ngeow, C. C., et al. 2011, *MNRAS*, 413, 2709, doi: [10.1111/j.1365-2966.2011.18342.x](https://doi.org/10.1111/j.1365-2966.2011.18342.x)
- Ting, Y.-S., Conroy, C., Rix, H.-W., & Cargile, P. 2019, *ApJ*, 879, 69, doi: [10.3847/1538-4357/ab2331](https://doi.org/10.3847/1538-4357/ab2331)
- Toledano, O., Moreno, E., Koenigsberger, G., Detmers, R., & Langer, N. 2007, *A&A*, 461, 1057, doi: [10.1051/0004-6361:20065776](https://doi.org/10.1051/0004-6361:20065776)
- Vida, K., & Roettenbacher, R. M. 2018, *A&A*, 616, A163, doi: [10.1051/0004-6361/201833194](https://doi.org/10.1051/0004-6361/201833194)
- Vidotto, A. A. 2021, *Living Reviews in Solar Physics*, 18, 3, doi: [10.1007/s41116-021-00029-w](https://doi.org/10.1007/s41116-021-00029-w)
- Vidotto, A. A., Gregory, S. G., Jardine, M., et al. 2014, *MNRAS*, 441, 2361, doi: [10.1093/mnras/stu728](https://doi.org/10.1093/mnras/stu728)
- Villarreal D’Angelo, C., Jardine, M., Johnstone, C. P., & See, V. 2019, *MNRAS*, 485, 1448, doi: [10.1093/mnras/stz477](https://doi.org/10.1093/mnras/stz477)
- Vincent, O., Bergeron, P., & Lafrenière, D. 2020, *AJ*, 160, 252, doi: [10.3847/1538-3881/abbe20](https://doi.org/10.3847/1538-3881/abbe20)
- Vogt, S. S., & Penrod, G. D. 1983, *PASP*, 95, 565, doi: [10.1086/131208](https://doi.org/10.1086/131208)
- Wang, J., Fu, J.-N., Zong, W., et al. 2020, *ApJS*, 251, 27, doi: [10.3847/1538-4365/abc1ed](https://doi.org/10.3847/1538-4365/abc1ed)
- Waugh, R. F. P., Jardine, M. M., Morin, J., & Donati, J. F. 2021, *MNRAS*, 505, 5104, doi: [10.1093/mnras/stab1709](https://doi.org/10.1093/mnras/stab1709)
- Wei, X. 2022, *ApJ*, 926, 40, doi: [10.3847/1538-4357/ac4755](https://doi.org/10.3847/1538-4357/ac4755)
- Wright, E. L., Eisenhardt, P. R. M., Mainzer, A. K., et al. 2010, *AJ*, 140, 1868, doi: [10.1088/0004-6256/140/6/1868](https://doi.org/10.1088/0004-6256/140/6/1868)
- Wu, Y., Du, B., Luo, A., Zhao, Y., & Yuan, H. 2014, in IAU Symposium, Vol. 306, Statistical Challenges in 21st Century Cosmology, ed. A. Heavens, J.-L. Starck, & A. Krone-Martins, 340–342, doi: [10.1017/S1743921314010825](https://doi.org/10.1017/S1743921314010825)
- Xing, K., Zong, W., Silvotti, R., et al. 2024, *ApJS*, 271, 57, doi: [10.3847/1538-4365/ad2ddd](https://doi.org/10.3847/1538-4365/ad2ddd)
- Xu, F., Gu, S., & Ioannidis, P. 2021, *MNRAS*, 501, 1878, doi: [10.1093/mnras/staa3793](https://doi.org/10.1093/mnras/staa3793)
- Zahn, J. P., & Bouchet, L. 1989, *A&A*, 223, 112
- Zaire, B., Donati, J. F., & Klein, B. 2021, *MNRAS*, 504, 1969, doi: [10.1093/mnras/stab1019](https://doi.org/10.1093/mnras/stab1019)
- . 2022, *MNRAS*, 513, 2893, doi: [10.1093/mnras/stac721](https://doi.org/10.1093/mnras/stac721)
- Zhang, B., Li, J., Yang, F., et al. 2021, *ApJS*, 256, 14, doi: [10.3847/1538-4365/ac0834](https://doi.org/10.3847/1538-4365/ac0834)
- Zong, W., Charpinet, S., Fu, J.-N., et al. 2018a, *ApJ*, 853, 98, doi: [10.3847/1538-4357/aaa548](https://doi.org/10.3847/1538-4357/aaa548)
- Zong, W., Fu, J.-N., De Cat, P., et al. 2018b, *ApJS*, 238, 30, doi: [10.3847/1538-4365/aadf81](https://doi.org/10.3847/1538-4365/aadf81)
- . 2020, *ApJS*, 251, 15, doi: [10.3847/1538-4365/abbb2d](https://doi.org/10.3847/1538-4365/abbb2d)